Long-wave-instability-induced pattern formation in an evaporating sessile or pendent liquid layer

Tao Wei and Fei Duan[*]

*School of Mechanical and Aerospace Engineering, Nanyang Technological University,
Singapore 639798, Singapore*

We investigate the nonlinear dynamics and stability of an evaporating liquid layer subject to vapor recoil, capillarity, thermocapillarity, ambient cooling, viscosity, and negative or positive gravity combined with buoyancy effects in the lubrication approximation. Using linear theory, we identify the mechanisms of finite-time rupture, independent of thermocapillarity and direction of gravity, and predict the effective growth rate of an interfacial perturbation which reveals competition among the mechanisms. A stability diagram is predicted for the onset of long-wave (LW) evaporative convection. In the two-dimensional simulation, we observe well-defined capillary ridges on both sides of the valley under positive gravity and main and secondary droplets under negative gravity, while a ridge can be trapped in a large-scale drained region in both cases. Neglecting the other non-Boussinesq effects, buoyancy does not have a significant influence on interfacial evolution and rupture time but makes contributions to the evaporation-driven convection and heat transfer. The average Nusselt number is found to increase with a stronger buoyancy effect. The flow field and interface profile jointly manifest the LW Marangoni-Rayleigh-Bénard convection under positive gravity and the LW Marangoni convection under negative gravity. In the three-dimensional simulation of moderate evaporation with a random perturbation, the rupture patterns are characterized by irregular ridge networks with distinct height scales for positive and negative gravity. A variety of interfacial and internal dynamics are displayed, depending on evaporation conditions, gravity, Marangoni effect, and ambient cooling. Reasonable agreement is found between the present results and the reported experiments and simulations. The concept of dissipative compacton also sheds light on the properties of interfacial fractalization.

I. INTRODUCTION

Interfacial instability and self-organized pattern formation of liquid layers have extensively been observed naturally and experimentally and explained theoretically and numerically over the past several decades. They still attract immense interest due to the intricate dynamics and significant roles in applications [1–3]. The physical mechanisms, such as capillarity, thermocapillarity, van der Waals (vdW) interaction, gravitational forces, and phase change, can be involved in the dynamics. However, even for the widely studied interfacial and convective instabilities in liquid layers, the role of buoyancy is not fully understood and debates persist on its interplay with thermocapillarity (see Refs. [4,5], for example). As is well known, the convection in the nonevaporating thin layers has been considered to be dominated by surface-tension-driven instability [6–8]. However, from the experiments of Zhang [9], (i) (0.5–1)-mm R-113 layers presented buoyancy-driven convection characteristics and (ii) high

---

[*]feiduan@ntu.edu.sg

volatility was significant for the Rayleigh-Bénard convection. It is suggested that the buoyancy effects really cannot be neglected even for a thin evaporating layer unless under the microgravitational conditions. As demonstrated in Ref. [10] with a water-water vapor equilibrium system, the ratio of their evaporation number to Rayleigh number is of the order of 10^{-2} for the liquid thickness of $h = 0.1$ mm, which characterizes the relative importance of mass loss and buoyancy.

Thermocapillary instability can be coupled with evaporation of pure liquid layers [11,12]. Chauvet *et al.* [12] proposed a concise theoretical model on phase-change-induced heat spreading along an interface with a thermal balance that includes a heat transfer coefficient $\alpha_I \|\boldsymbol{q}\|$ depending on the wave number $\|\boldsymbol{q}\|$ of the fluctuation in surface temperature θ_I. The mechanism homogenized θ_I and hence mitigated Marangoni flows. Then their theory was validated by accurately measuring the critical conditions of the evaporative Bénard-Marangoni (BM) convection in liquid layers of hydrofluoroether (HFE) with $h \lesssim 1$ mm [12]. Besides the short-wave (SW) hexagonal (or BM) mode for a flat interface studied in the absence (e.g., Refs. [6,13,14]) or presence (e.g., Refs. [12,15,16]) of evaporation, the long-wave (LW) deformational Marangoni instability has been widely investigated as well, where the surface deformation plays a crucial role. With the linear stability analysis (LSA) it was first explained by Scriven and Sternling [17] in the absence of gravity (just like the work of Pearson [6]) and then extended by Smith [18]; the latter found that surface gravity wave was important for LW, which was later observed quantitatively in the experiments [7,8,19]. Burelbach *et al.* [19] demonstrated the thermocapillary flow in a nonuniformly heated silicone-oil layer. They found that the profiles agreed with the prediction of long-wave theory provided the substrate temperature θ_w was not too high and the film was not close to rupture and that thermocapillarity was less effective when evaporation was present. VanHook *et al.* [7] performed experiments on the onset and exchange of LW and SW instabilities in the confined, thin silicone-oil–gas system subject to a vertical temperature gradient. Later, they observed the LW Marangoni convection and found that the formation of localized depression or elevation depended on the thickness and thermal conductivity of a gas layer [8]. To improve the predictions, they developed an evolution equation including a "two-layer" Biot number to account for the effect of deformation on heat transfer [8]. After the pioneering prediction of Smith [18] on the possible coexistence or competition between the two modes at threshold, Golovin *et al.* [20–22] systematically studied the interaction between the short-scale BM convection and the LW deformation instability.

Thermocapillary and buoyancy effects can simultaneously affect the evaporative convection in a thick layer [11] and even in certain thin ones [9,10]. Berg *et al.* [11] performed the earliest exploratory experiments on evaporating pure liquids. Using the schlieren technique, they observed various surface convective patterns dependent mainly on thickness and volatility. Zhang [9] conducted experiments on volatile layers of ethanol and R-113 ($h \leqslant 1$ mm) and considered evaporation itself as a motivity of the convective instabilities and defined the generalized Marangoni and Rayleigh numbers as the onset criteria. The buoyancy mechanism was shown to play an important role in the flow patterns of a highly volatile liquid (R-113) whether the layers were heated or cooled from below provided the temperature difference between the bottom and free surface was positive [9]. Therefore, it is reasonable to incorporate both the thermocapillary and buoyancy effects in a finite-thickness (but still thin compared with LW disturbances) evaporating layer in the nonlinear regime.

Since buoyancy will be introduced through the Boussinesq approximation, it is essential for the validity of the approach based on the Boussinesq model equation [Eq. (2)]. As reemphasized in Ref. [23], in order for this approximation to be valid for the heated layers, $\varepsilon = \beta \Delta\theta$ must be small ($\ll 1$) and Ra $\ll$ Ga, where β (>0) is the volume thermal expansion coefficient of the liquid and $\Delta\theta$ is the characteristic temperature difference across the layer; the definitions of the dimensionless parameters are presented in Table I. With the parameters used in our model, an equivalent requirement is that $|\mathrm{Ga}| = |G|\mathrm{Pr} = |\mathrm{Ra}|/\varepsilon \gg 1$, where the absolute-value sign is for the pendent configuration of Rayleigh-Taylor instability, and thus $|\mathrm{Ra}| \ll |G|\mathrm{Pr}$ or $|\mathrm{Gr}| \ll |G|$. Accordingly, we emphasize that the parameter set of the system should satisfy the validity conditions to obtain physically acceptable results, as chosen in this study. This issue will be reiterated after introducing the model in Sec. III A

TABLE I. Definitions and physical meanings of relevant dimensionless quantities.

Dimensionless group	Definition	Physical meaning
Galileo number	$\mathrm{Ga} = \frac{\tau_{\mathrm{visc}}\tau_{\mathrm{th}}}{\tau_{\mathrm{grav}}^2} = \frac{gh_0^3}{\alpha\nu}$	ratio of the product of viscous and thermal diffusive time scales ($\tau_{\mathrm{visc}} = \frac{h_0^2}{\nu}$ and $\tau_{\mathrm{th}} = \frac{h_0^2}{\alpha}$) to the square of gravitational time scale $\tau_{\mathrm{grav}} = \sqrt{h_0/g}$, where $\alpha = k_{\mathrm{th}}/\rho c_p$ is the liquid thermal diffusivity
Rayleigh number	$\mathrm{Ra} = \frac{\tau_{\mathrm{visc}}\tau_{\mathrm{th}}}{\tau_{\mathrm{b}}^2} = \frac{gh_0^3\beta\Delta\theta}{\alpha\nu}$	ratio of the product of τ_{visc} and τ_{th} to the square of buoyant time scale $\tau_{\mathrm{b}} = \sqrt{h_0/g\beta\Delta\theta}$
Prandtl number	$\mathrm{Pr} = \frac{\tau_{\mathrm{th}}}{\tau_{\mathrm{visc}}} = \frac{\nu}{\alpha}$	momentum diffusion rate relative to heat conduction
Grashof number	$\mathrm{Gr} = \frac{\mathrm{Ra}}{\mathrm{Pr}} = \frac{gh_0^3\beta\Delta\theta}{\nu^2}$	measure of buoyancy as Ra, but divided by Pr
gravity number	$G = \frac{\tau_{\mathrm{visc}}^2}{\tau_{\mathrm{grav}}^2} = \frac{gh_0^3}{\nu^2}$	square of ratio of τ_{visc} to τ_{grav}, a measure of gravity
static Bond number	$\mathrm{Bo} = \frac{1}{3}\frac{|G|}{\Sigma_0} = \frac{\rho|g|h_0^2}{\sigma_0}$	comparison of gravitational force to surface tension
dynamic Bond number	$\mathrm{Bo}_d = \frac{\mathrm{Ra}}{\mathrm{Ma}} = \frac{2\rho gh_0^2}{\gamma}$	measure of the relative strength of buoyancy to thermocapillary forces
surface-tension number	$\Sigma_0 = \frac{h_0\sigma_0}{3\rho\nu^2}$	measure of the surface deformation: large values of Σ_0 (or σ_0) allow a small surface deformation
Marangoni number	$\mathrm{Ma} = \frac{\tau_{\mathrm{visc}}\tau_{\mathrm{th}}}{\tau_{\mathrm{tc}}^2} = \frac{\gamma\Delta\theta h_0 c_p}{2\nu k_{\mathrm{th}}}$	ratio of the product of τ_{visc} and τ_{th} to the square of thermocapillary time scale $\tau_{\mathrm{tc}} = \sqrt{\rho h_0^3/\gamma\Delta\theta}$
crispation number	$C = \frac{\gamma\Delta\theta}{\sigma_0}$	comparison of thermocapillary force to surface tension
density ratio	$D = \frac{3}{2}\frac{\rho_g}{\rho}$	measure of the ratio of gas to liquid densities
dimensionless latent heat	$L = \frac{8}{9}\frac{h_0^2\tilde{L}}{\nu^2}$	measure of the latent heat
evaporation number	$E = \frac{\tau_{\mathrm{visc}}}{\tau_{\mathrm{ev}}} = \frac{k_{\mathrm{th}}\Delta\theta}{\nu\rho\tilde{L}}$	ratio of τ_{visc} to evaporative time scale $\tau_{\mathrm{ev}} = \rho h_0^2\tilde{L}/k_{\mathrm{th}}\Delta\theta$, a measure of the rate of mass loss ($0 < E \ll 1$ for weak and moderate evaporation), slightly different from the expression in Ref. [10]
nonvolatile Biot number	$\mathrm{Bi} = \frac{h_0 h_{\mathrm{th}}}{k_{\mathrm{th}}}$	measure of the sensible heat losses into ambient cooling
nonequilibrium parameter	$K = \frac{\tilde{K}k_{\mathrm{th}}}{h_0\tilde{L}}$	measure of nonequilibrium degree at interface
local Nusselt number	$\mathrm{Nu} = \frac{h_{\mathrm{th}}^{(l)}h_{\mathrm{av}}}{k_{\mathrm{th}}}$	ratio of the total heat flux across the layer to the conductive flux

and in Sec. VII. In addition, the buoyancy effect along with the Boussinesq approximation can be left out of the model by setting Ra = 0 as $\varepsilon \to 0$.

When a liquid layer is suspended under a substrate, the configuration is potentially unstable to infinitesimal deformations of the interface, known as the Rayleigh-Taylor problem [24]. A series of $(1 + 1)$-dimensional [$(1 + 1)$D] patterns of LW pendent droplets separated by drained regions was shown in Ref. [25]. The $(1 + 1)$D Rayleigh-Taylor patterns have also been investigated for the case of a viscous layer overlaid by another immiscible fluid with a larger density [26]. Here and in the following $(1 + 1)$ and $(2 + 1)$ denote the numbers of independent spatial plus temporal variables in a thin-film equation, which give two and three physical dimensions of the problem studied, respectively. Fermigier *et al.* [27] demonstrated the formation and transition of $(2 + 1)$D patterns in the suspended silicone-oil layers. However, for Rayleigh-Taylor instability (RTI) in evaporating layers, relevant analyses on $(2 + 1)$D pattern formation are still lacking. With localized evaporation and condensation, Bestehorn and Merkt [28] showed that such a layer could be stabilized and rupture was avoided even without stabilizing thermocapillarity. However, they neglected vapor recoil, which is an intrinsic effect of evaporation in favor of interfacial and convective instabilities [29,30]. It has been found that

the destabilization of vapor recoil has an increasing influence on the dynamics approaching rupture [31,32], which is also tangibly recognizable for rapid evaporation under reduced pressure [30]. Prosperetti and Plesset [33] revisited the problem without Marangoni effect and viscosity, stating that the destabilizations of vapor recoil, inertia [30], and a moving boundary were all negligible. Nevertheless, confirmation of the above theories is prevented due to the absence of a relevant precise experiment. In this study we investigate the influences of vapor recoil and thermocapillarity arising from nonequilibrium evaporation on the morphology of Rayleigh-Taylor unstable layers and explain the differences from the results in Ref. [28].

A nonlinear model for evaporating ultrathin (10–100 nm) film was proposed by Burelbach *et al.* [31] with the LW theory. Under a one-sided assumption, they derived and solved numerically a $(1 + 1)$D evolution equation with the effects of nonequilibrium, thermocapillarity, vdW attractions, mass loss, and vapor recoil taken into account. Joo *et al.* [34] extended the model to an evaporating layer falling down an inclined plate. Oron [35] considered $(2 + 1)$D evaporating films with a special intermolecular potential. Shklyaev and Fried [36] generalized the model with more general interface conditions. Some works on interfacial instability due to evaporation have considered a bilayer system [10,37–39]. Most such studies focused on a linear or weakly nonlinear analysis except for that of Kanatani and Oron [39], who considered a nonlinear evolution of a confined liquid-vapor system but neglected mass loss or gain and vapor recoil due to the dominant effect of vapor pressure. We note that the attention to the potential effect of vapor recoil on the rupture dynamics was not paid in the subsequent studies succeeding Refs. [31,34,36]. Therefore, further discussion of the vapor-recoil instability and its interaction with the Marangoni and mass-loss effects is within the scope of the present study. Furthermore, the thinness of evaporating layers causes considerable difficulties in obtaining reliable experimental results of convection patterns. Most nonlinear studies explained the interfacial dynamics without internal convection, except Refs. [8,40–42] provided physical insights into the bulk flow of a liquid layer but without evaporation. Thus, it would be interesting to correlate surface deformations with convection manifestations of the evaporation dynamics driven by the aforementioned mechanisms.

The heat flux on the vapor side of an evaporating interface comprises the sensible and latent heat, which can be included readily in an interfacial energy balance. As noted by Burelbach *et al.* [19] in (1–2)-mm silicone-oil layers with a high θ_w, a nearly 40% underestimate of the minimum thickness from the one-sided model was due to the neglect of cooling by thermal convection or diffusion through gas besides the latent heat consumption. Although our study does not directly deal with the heat and mass transfer in the gas phase, we give qualitative predictions on how the destabilizing mechanisms and dynamics, e.g., thermocapillarity, rupture time t_r, and characteristic scales, are modified by a phenomenological heat-transfer coefficient to shed light on the discrepancy between the experiment and the simulation in Ref. [19], which pertains to sensible heat that the liquid must release. On the other hand, intensive heat losses cause the liquid temperature near the free surface to be lower than that of the heated interior, thus buoyancy due to adverse density gradient is naturally expected to play a role [15,25,43]. In the framework of the one-sided model, a well-defined heat transfer coefficient was related to a wave-number-dependent effective Biot number [16] through $\mathrm{Bi}_{\mathrm{eff}} = \alpha_I k$ in Ref. [12], where the dimensionless wave number $k = \|\boldsymbol{q}\| h$. At a large value of α_I, interfacial temperature homogenization mitigates Marangoni flows in favor of buoyancy instability [12,43]. This mechanism motivates us to incorporate both the heat transfer coefficient and buoyancy effect. Physically, convection driven by buoyancy provides an additional perturbation source for the interface [30], which may influence the local dynamics of the thickened region with a sufficient temperature gradient. This issue has not been investigated based on LW theory. Relevant experimental data (far from threshold, $k \ll k_c$) is also very limited, which renders a direct comparison difficult. The differences between our simulations and the nonevaporating experiments of VanHook *et al.* [7,8] will be explained instead.

It should be noted that there is another important body of work that concerns the self-similar solutions describing (i) the finite-time singularities *near* rupture [44–48] and (ii) the hierarchical structure of stationary profiles created by an *infinite* series of rupture events [49–51]. The former
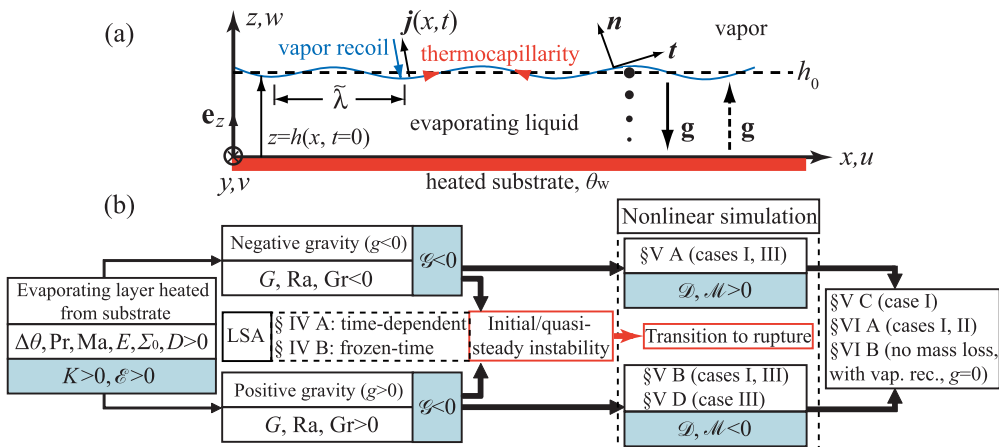
FIG. 1. (a) Schematic of an unstable evaporating liquid layer subject to gravity combined with buoyancy, covering a heated horizontal substrate with surface wavelength $\tilde{\lambda} \gg h_0$. Here $\mathbf{g} = -g\mathbf{e}_z$, $\mathbf{e}_z$ is the unit vector in the z direction, an arrow with a solid line shows $g > 0$, and an arrow with a dashed line shows $g < 0$. The smaller dot in the layer denotes a lighter fluid particle. (b) Cases considered and study outline.

focused on the stability and structure of time-developing vdW rupture without gravity and most under thermal equilibrium (i.e., no evaporation and thermocapillarity). However, the studies of the latter are relatively few in the film context, among which Shklyaev *et al.* [49] introduced a dissipative compacton (DC), which is a stationary analog of the usual compacton [52] with compact support, emerging from systems with nonlinear dissipation. Physically, a DC can describe a stationary single-drop solution with zero microscopic contact angle, which is energetically favored on the basis of a Lyapunov functional [49,50]. By extending the DC to include the vapor-recoil effect, we quantitatively characterize the properties of an interfacial fractal. Recently, the dynamics of rupture in a generalized mathematical model of thin films of viscous fluids with the modified evaporative effects has included the study of self-similar solutions as well [53].

In this study we extend the work of Burelbach *et al.* [31] by incorporating the effects of gravity combined with buoyancy and ambient cooling for further understanding and predicting the flow field and pattern formation of a finite-thickness evaporating layer. Oron [35,54] adopted random disturbances and indicated that a $(2 + 1)$D simulation [45] was indispensable to the study of film dynamics. We also use random perturbations in $(2 + 1)$D simulations to corroborate the generalized model. The results are compared with relevant experiments and simulations. Recently, the comparison of standard asymptotic thin-film models, variational thin-film models, and Stokes calculations illustrates the power of the gradient-dynamics approach as compared to the standard asymptotics [55]. Thus, a further aim is to cast the dynamic equations incorporating a mass flux term into a gradient dynamics form that combines the conserved and nonconserved terms (see Appendix C).

II. MATHEMATICAL FORMULATION

We consider a laterally unbounded, Newtonian, and volatile liquid layer bounded from above (below) by an interface with a semi-infinite vapor of far-field saturation temperature θ_s and below (above) by a rigid, conducting, horizontal substrate maintained at a constant temperature θ_w ($>\theta_s$), in the case of positive (negative) gravity. The physical properties of the liquid are taken as constant at the reference temperature θ_s except for surface tension and density. The surface tension is represented as $\sigma = \sigma_0 - \gamma(\theta - \theta_s)$, where $\sigma_0 = \sigma(\theta_s)$ and $\gamma \equiv -(d\sigma/d\theta)|_{\theta_s} > 0$.

The system is formulated with Cartesian coordinates (x, z) with an unperturbed mean thickness h_0, as shown in Fig. 1(a). This model can be extended straightforwardly to a $(2 + 1)$D case, in which

x and y coordinates are parallel to the substrate. The gas-liquid interface height $z = h(x,t)$ is a function of x and time t. The unit vector normal to the interface and directed towards the gas phase is expressed as $\mathbf{n} = (-h_x, 1)/\sqrt{1 + h_x^2}$, while $\mathbf{t} = (1, h_x)/\sqrt{1 + h_x^2}$ represents the unit vector tangent to the interface. The subscripts pertaining to independent variables denote partial differentiation throughout this paper. Moreover, a reference body force $\mathbf{F}_{RB} = -\nabla\phi$, with a gravitational potential $\phi = \rho g z$ per unit volume, is defined to take buoyancy in liquid into account, where $\nabla = (\partial_x, \partial_z)$ is the gradient, ρ the liquid reference density at θ_s, and g the acceleration due to gravity. Using the Boussinesq approximation (ruling out compressibility and temperature dependence of the bulk liquid properties other than density, i.e., non-Boussinesq effects [23]), the momentum, continuity, and energy equations for the fluid flow read

$$\rho(u_t + \mathbf{v} \cdot \nabla u) = -p_x + \mu\nabla^2 u, \tag{1}$$

$$\rho(w_t + \mathbf{v} \cdot \nabla w) = -p_z + \mu\nabla^2 w - \rho[1 - \beta(\theta - \theta_s)]g, \tag{2}$$

$$\nabla \cdot \mathbf{v} = 0, \quad \rho c_p(\theta_t + \mathbf{v} \cdot \nabla\theta) = k_{th}\nabla^2\theta, \tag{3}$$

where ∇^2 is the Laplacian, $\mathbf{v} = (u,w)$ for the velocity, and p is the pressure of liquid relative to the vapor. The liquid properties μ, c_p, and k_{th} are dynamic viscosity, heat capacity, and thermal conductivity, respectively. Variations in density are assumed to be brought about only by a moderate temperature difference and are incorporated only in the buoyancy term of Eq. (2).

At the liquid-solid interface $z = 0$, we apply the Dirichlet conditions $u = w = 0$ and $\theta = \theta_w$. At the gas-liquid interface $z = h(x,t)$, the mass balance reads $j = \rho(\mathbf{v} - \mathbf{v}_I) \cdot \mathbf{n} = \rho_g(\mathbf{v}_g - \mathbf{v}_I) \cdot \mathbf{n}$; hereafter the subscripts g and I refer to the quantities pertaining to gas phase and interface. That $\frac{\rho_g}{\rho} = O(10^{-3})$ implies that the normal velocity evaluated on the gas side of the interface is much larger than that of the liquid side. The interfacial energy balance then takes the form

$$j\left\{\tilde{L} + \tfrac{1}{2}[(\mathbf{v}_g - \mathbf{v}_I) \cdot \mathbf{n}]^2 - \tfrac{1}{2}[(\mathbf{v} - \mathbf{v}_I) \cdot \mathbf{n}]^2\right\} + k_{th}\nabla\theta \cdot \mathbf{n} + h_{th}(\theta - \theta_s) = 0, \tag{4}$$

where $\tilde{L}$ denotes the latent heat and viscous heating is omitted. The last term expresses the conductive or convective heat flux in the gas [9] by a global heat-transfer coefficient h_{th} [56] because our major concern is the dynamics of liquid instead of a detailed description of the heat and mass transfer per se. Basically, it provides an additional mechanism of energy transfer neglected in Refs. [31,34,57]. In the presence of phase change, the interfacial stress balance reads

$$j[(\mathbf{v} - \mathbf{v}_I) - (\mathbf{v}_g - \mathbf{v}_I)] - \mathbf{n} \cdot (\mathsf{T} - \mathsf{T}_g) = -2\kappa\sigma\mathbf{n} - \nabla_s\sigma, \tag{5}$$

where T is the stress tensor, ∇_s the surface gradient, and κ the mean curvature.

At the fluid across the interface $F(x,z,t) = z - h(x,t) = 0$, its kinematic condition is

$$j = \rho(w - h_t - uh_x)(1 + h_x^2)^{-1/2}. \tag{6}$$

Then j is related to the local interface temperature by the modified Hertz-Knudsen law [30]

$$\tilde{K}j = \theta_I - \theta_s \equiv \Delta\theta_I.$$

In quasiequilibrium $\Delta\theta_I = 0$, the interface is in thermal equilibrium; for a net mass transfer, a vapor pressure driving force must exist, represented as the nonequilibrium parameter $\tilde{K} = \theta_s^{3/2}(a\rho_g\tilde{L})^{-1}\sqrt{\frac{2\pi R_g}{M_w}}$ [1,31]. Here R_g is the universal gas constant, M_w is the molecular weight, and a is the accommodation coefficient ($0 < a \leqslant 1$). Physically, $\tilde{K}$ characterizes the volatility of a liquid [31], harder to volatilize with increasing $\tilde{K}$. Intuitively, it can be expected that $\tilde{K}$ has a stabilizing effect, indeed shown by LSA in Sec. IV, while its unexpected dual role is found in the nonlinear regime (Sec. V C). In the quasiequilibrium limit $\tilde{K} \to 0$, $\theta_I \to \theta_s$, corresponding to $\omega_I \to 1$ in Eq. (5) of Ref. [12], with ω_I being the molar fraction of surface vapor (cf. the remark

in Appendix B). Thus, $\tilde{K}^{-1}$ could potentially account for the effect of evaporation-induced thermal diffusion along the interface as a function of ω_I [12].

We adopt the one-sided approximation $\rho_g \ll \rho$ and $\mu_g \ll \mu$ to decouple the dynamics of liquid from gas, but never apply $k_{th,g} \ll k_{th}$ [9,56,58]. It generalizes that used in Ref. [31], where a nonevaporating film would be isothermal due to the absence of conduction and convection heat fluxes in the gas. Our treatment of the surrounding gas as being inviscid but heat conducting is also justified by the order-of-magnitude analysis [33]. For a finite-thickness silicone oil, ethanol, or methanol layer covered with a helium atmosphere, the helium thermal conductivity (0.153 W m^{-1} K^{-1}) is close to that of the liquid with the value of 0.133, 0.153, or 0.190 W m^{-1} K^{-1}. Under this circumstance the cooling effect of gas on the liquid dynamics should be significant, e.g., the experiments with $h \approx 0.3$ mm silicone oil under the helium gas [8]. In our model, the gas phase thus exerts a force in the form of vapor thrust and acts as a heat sink. With a similar manipulation in Ref. [31], Eqs. (4) and (5) are reduced to

$$j\left[\tilde{L} + \tfrac{1}{2}\left(j\rho_g^{-1}\right)^2\right] + h_{th}(\theta - \theta_s) = -k_{th}\nabla\theta \cdot \mathbf{n}, \tag{7}$$

$$j^2 \rho_g^{-1} + \mathbf{n} \cdot \mathsf{T} \cdot \mathbf{n} = 2\kappa\sigma, \quad \mathbf{n} \cdot \mathsf{T} \cdot \mathbf{t} = \nabla_s \sigma \cdot \mathbf{t}. \tag{8}$$

Equation (7) means that the thermal energy conducted to the interface is converted to the latent heat, the heat losses into surroundings, and the kinetic energy of vapor particles. Finally, the mathematical formulation consists of the governing equations (1)–(3), the Dirichlet conditions for the wall, and the free-surface conditions shown in Eqs. (6)–(8) and incorporates additional mechanisms in addition to those discussed by Burelbach *et al.* [31], (i) energy flux arising from *ambient cooling* and (ii) *gravity* in combination with *buoyancy* effects, but the vdW attractions are neglected due to the finite thickness.

We then introduce the scalings for principal dimensionless variables

$$(X,Z,H) = h_0^{-1}(x,z,h), \quad T = h_0^{-2}\nu t, \quad (U,W) = h_0 \nu^{-1}(u,w),$$
$$(P,\Phi) = h_0^2 \rho^{-1}\nu^{-2}(p,\phi), \quad J = \tilde{L}h_0(k_{th}\Delta\theta)^{-1}j, \quad \Theta = \Delta\theta^{-1}(\theta - \theta_s), \tag{9}$$

where ν is kinematic viscosity and $\Delta\theta = \theta_w - \theta_s$. The viscous scales have been justified in a nonisothermal film subject to capillarity, thermocapillarity, viscosity, and vdW attractions when evaporation was not very intense [31]; thus they should be appropriate for a layer subject to gravity as well. The nondimensionalization yields the dimensionless groups, listed in Table I. Substitution of the scalings in Eq. (9) into Eqs. (1)–(3) yields

$$U_T + UU_X + WU_Z = -P_X + U_{XX} + U_{ZZ}, \tag{10}$$

$$W_T + UW_X + WW_Z = -(P + \Phi)_Z + W_{XX} + W_{ZZ} + \mathrm{Gr}\Theta, \tag{11}$$

$$U_X + W_Z = 0, \quad \mathrm{Pr}(\Theta_T + U\Theta_X + W\Theta_Z) = \Theta_{XX} + \Theta_{ZZ}, \tag{12}$$

where the reference potential function is $\Phi = GZ$. At $Z = 0$, the scaled boundary conditions (BCs) are $U = W = 0$ and $\Theta = 1$. At $Z = H(X,T)$, the BCs become

$$J + (E^2 D^{-2} L^{-1})J^3 + \mathrm{Bi}\Theta = (\Theta_X H_X - \Theta_Z)\left(1 + H_X^2\right)^{-1/2}, \tag{13a}$$

$$\tfrac{3}{2}E^2 D^{-1}J^2 - P + 2\left[U_X\left(H_X^2 - 1\right) - H_X(W_X + U_Z)\right]\left(1 + H_X^2\right)^{-1}$$
$$= 3\Sigma_0 H_{XX}(1 - C\Theta)\left(1 + H_X^2\right)^{-3/2}, \tag{13b}$$

$$(U_Z + W_X)\left(1 - H_X^2\right) - 4U_X H_X = -2\,\mathrm{Ma}\,\mathrm{Pr}^{-1}(\Theta_X + \Theta_Z H_X)\left(1 + H_X^2\right)^{1/2}, \tag{13c}$$

$$EJ = (W - H_T - UH_X)\left(1 + H_X^2\right)^{-1/2}. \tag{13d}$$

The vapor thrust, represented by the first term on the left-hand side of Eq. (13b), can be regarded as an externally imposed normal stress. The scaled constitutive equation is

$$KJ = \Theta_I. \tag{14}$$

The $O(1)$ basic-state solution to the system (10)–(14) can be straightforwardly obtained and is given in Appendix A. To put our modification of the thermal boundary condition in the context of earlier studies, it is helpful to discuss the effects of ambient cooling in the nonvolatile ($K \to \infty$), quasiequilibrium and nonequilibrium cases ($K = 0$ and $K > 0$). Noted that Θ_I depends on local mass flux under nonequilibrium.

In the nonvolatile limit of $J \to 0$, $K \to \infty$ is suggested by a nonzero value of Θ_I in Eq. (14). Note that $\Theta_I = 1$ in the framework of Refs. [31,34], while $0 < \Theta_I < 1$ in our model due to the convective and conductive heat flux on a free surface. The condition (13a) subsequently reduces to $\text{Bi}\Theta = -\Theta_\mathbf{n}$ instead of discarding the definition of K and redefining K^{-1} as a surface Biot number for the nonvolatile case. On the other hand, with $J > 0$, $K \to 0$ is implied by Eq. (14) due to $\Theta_I \to 0$ ($\theta_I \to \theta_s$) under the quasiequilibrium limit. Equation (13a) becomes $J + \frac{E^2}{D^2 L} J^3 = -\Theta_\mathbf{n}$, suggesting that the heat flow by convection and conduction on the gas side of the interface is negligible in comparison with that arising from quasiequilibrium evaporation. Due to the insignificance of ambient cooling, one can set $\text{Bi} \to 0$ for simplicity and expect that the evaporation effects of mass loss and vapor recoil together with the other destabilizing mechanisms (e.g., RTI and the Marangoni effect) would be adequate for the onset of LW instability. This simplification is also supported by the relatively intense evaporation under quasiequilibrium [32] and a similar case considered by Palmer [30]. Physically, the sensible heat loss can also play the role of dissipative mechanism for the nonequilibrium case rather than only for the nonvolatile case where K acts as an inverse Biot number [34]. Thus, K^{-1} could be considered as an interfacial heat-transfer coefficient associated with phase change, which impacts the dynamics together with Bi (cf. Appendix B). Therefore, the ambient cooling should be examined in the nonequilibrium case of a lower evaporation rate [9,56,58]. The provision is distinct from, but not inconsistent with, the cases discussed in Ref. [31].

III. EVOLUTION EQUATION AND NUMERICAL IMPLEMENTATION

We now develop a strongly nonlinear model governing the motion of the gas-liquid interface based on LW asymptotics, reiterate its validity conditions, and present a numerical method to solve the model for the time evolution of instabilities.

A. Evolution equation based on long-wave theory

We assume that the spatiotemporal variations of the dependent variables of the system (10)–(14) are slow enough to justify the lubrication approximation [1]. We consider the LW disturbance of a characteristic length $\tilde{\lambda}$ in the x direction by introducing a small wave number $k = 2\pi h_0/\tilde{\lambda}$. The derivation of the evolution equation mostly follows the approach in Ref. [59] with the lubrication variables $\xi = kX$, $\zeta = Z$, and $\tau = kT$, but with modifications relevant to the present work. In particular, to incorporate the effects of gravity accompanied by buoyancy, we let $G, \text{Ra} = O(k^{-1})$ to make them comparable to the pressure term along with the additional constraint $|\text{Gr}| \ll |G|$ for validity of the Boussinesq model equation (see Sec. I). Then we define the asymptotic transformation

$$(D, E, G, \text{Ma}, \text{Ra}, \Sigma_0) = (\bar{D}k^3, \bar{E}k, \bar{G}k^{-1}, \bar{M}k^{-1}, \bar{R}k^{-1}, \bar{\Sigma}_0 k^{-3}). \tag{15}$$

The quantities with overbars are $O(1)$ as $k \to 0$ in order to preserve the effects of vapor recoil, mass loss, gravity, thermocapillarity [Pr, $K = O(1)$], buoyancy, and surface tension at leading order. To make the effects of heat flow between ambient gas and free surface enter the

analysis, we set $\mathrm{Bi} = O(1)$. The dependent variables are expanded for small k, $(U, W, J, \Theta, P) = (U_0, kW_0, J_0, \Theta_0, k^{-1}P_0) + k(U_1, kW_1, J_1, \Theta_1, k^{-1}P_1) + \cdots$, where the subscript 0 denotes $O(1)$ quantities. We then obtain the $O(1)$ governing equations from (10)–(12),

$$0 = -\partial_\xi P_0 + \partial_\zeta^2 U_0, \tag{16}$$

$$0 = -\partial_\zeta P_0 - (\bar{G} - \bar{R}\mathrm{Pr}^{-1}\Theta_0), \tag{17}$$

$$H_\tau + \partial_\xi \int_0^H U_0 d\zeta + \bar{E}J_0 = 0, \tag{18}$$

$$0 = \partial_\zeta^2 \Theta_0, \tag{19}$$

where $H(\xi, \tau)$ is an undetermined $O(1)$ function. The conservation form of kinematic equation (18) is obtained by integrating the continuity equation, implying the slaving of the flow field to surface kinematics under the assumption of a low Reynolds number. The BCs at $\zeta = 0$ read $U_0 = W_0 = 0$ and $\Theta_0 = 1$, while at $\zeta = H$,

$$\bar{E}J_0 = -H_\tau - U_0 H_\xi + W_0, \tag{20a}$$

$$J_0 + \mathrm{Bi}\Theta_0 = -\partial_\zeta \Theta_0, \tag{20b}$$

$$\tfrac{3}{2}\bar{E}^2 \bar{D}^{-1} J_0^2 - P_0 = 3\bar{\Sigma}_0 H_{\xi\xi}, \tag{20c}$$

$$\partial_\zeta U_0 = -2\bar{M}\mathrm{Pr}^{-1}(\partial_\xi \Theta_0 + H_\xi \partial_\zeta \Theta_0), \tag{20d}$$

$$KJ_0 = \Theta_0. \tag{20e}$$

The procedure to obtain a $(1 + 1)$D evolution equation is standard [1]. The $O(1)$ solution of Eqs. (16)–(20) is detailed in Appendix B, which modifies that of Burelbach *et al.* [31] by the existence of gravity combined with buoyancy and ambient cooling. Finally, the governing system is collapsed into the equation for $H(X, T)$,

$$H_T + EJ_0 + \Sigma_0(H^3 H_{XXX})_X - \tfrac{1}{3}G(H^3 H_X)_X + [H^2 H_X f J_0(K\,\mathrm{Ma}\,\mathrm{Pr}^{-1} + E^2 D^{-1} H J_0)]_X$$
$$+ \tfrac{1}{3}\mathrm{Gr}[H^3 H_X - \tfrac{1}{2}H^3(H^2 f)_X + \tfrac{9}{40}H^5 f_X]_X = 0, \tag{21}$$

where $f(H) = \frac{1+\mathrm{Bi}K}{K+(1+\mathrm{Bi}K)H}$. Within the LW regime $\mathrm{Bo} = \frac{|\bar{G}|k^{-1}}{3\bar{\Sigma}_0 k^{-3}} = O(k^2) \ll 1$ as $k \to 0$, Eq. (21) will be a valid limit to the governing system in an excluded time interval since the lubrication assumption breaks down near $T = 0$ and the basic-state disappearance time T_e (cf. Appendix A). The second and fourth terms account for mass loss and gravity. Capillary force stabilizes the interface through the dissipation term of the fourth-order derivative. The fifth term is associated with thermocapillarity and vapor recoil. In contrast, the polynomial in the second set of square brackets describes the driving forces of convection due to buoyancy with the functions of H multiplied by H^n, accentuated (attenuated) in the thicker (thinner) region. As $K \to 0$ the Marangoni instability is absent, according with Refs. [12,16]. When $K \to \infty$ and $E = 0$, it governs the LW instability of nonvolatile viscous layers. Further, the buoyancy effect is also eliminated ($\mathrm{Gr} = 0$), a case that has been studied intensively [7,8,25,40,42,54,60]. With a proper vdW potential and $G, \mathrm{Gr}, \mathrm{Bi} \to 0$, one can recover the model for ultrathin films with molecular interactions [31,61]. Assuming that all forces are isotropic in the horizontal dimensions and that ∂_X and ∂_Y are comparable since the perturbation has no preferred direction, it is easy to generalize Eq. (21) as a $(2 + 1)$D version

$$H_T + EJ_0 + \Sigma_0\nabla_1 \cdot [H^3\nabla_1(\nabla_1^2 H)] + \nabla_1 \cdot [H^2 f J_0(K\,\mathrm{Ma}\,\mathrm{Pr}^{-1} + E^2 D^{-1} H J_0)\nabla_1 H]$$
$$- \tfrac{1}{3}G\nabla_1 \cdot (H^3\nabla_1 H) + \tfrac{1}{3}\mathrm{Gr}\nabla_1 \cdot [H^3\nabla_1 H - \tfrac{1}{2}H^3\nabla_1(H^2 f) + \tfrac{9}{40}H^5\nabla_1 f] = 0, \tag{22}$$

where $\nabla_1 = (\partial_X, \partial_Y)$ is the component of the spatial gradient parallel to the substrate and ∇_1^2 is the corresponding Laplacian.

To make the presentation of numerical results more concise, we introduce the rescalings

$$(\hat{x}, \hat{y}) = \sqrt{|B|/\Sigma_0}(X, Y) = \sqrt{\text{Bo}}(X, Y), \quad \hat{t} = B^2 T/\Sigma_0, \tag{23}$$

with $B \equiv -\frac{1}{3}G$ for convenience, to absorb the parameters G and Σ_0 into the new groups

$$\mathscr{E} = \frac{E\Sigma_0}{B^2} = \frac{3k_{\text{th}}\Delta\theta\sigma_0\nu}{h_0^5(\rho g)^2\tilde{L}}, \quad \mathscr{M} = \frac{\text{Ma}}{B\text{Pr}} = \frac{-3\gamma\Delta\theta}{2h_0^2\rho g}, \quad \mathscr{D} = \frac{E^2}{BD} = \frac{-2k_{\text{th}}^2\Delta\theta^2}{h_0^3\rho_g\rho g\tilde{L}^2},$$

$$\mathscr{G} = \frac{\text{Gr}}{B} = -3\beta\Delta\theta, \tag{24}$$

then recast (22) into the canonical form (see Appendix C for relevant variational structures),

$$H_{\hat{t}} + \mathscr{E}J_0 + \hat{\mathbf{V}}_1 \cdot \left[H^3\hat{\mathbf{V}}_1\left(\hat{\nabla}_1^2 H\right)\right] \pm \hat{\mathbf{V}}_1 \cdot (H^3\hat{\mathbf{V}}_1 H) \pm \hat{\mathbf{V}}_1 \cdot [H^2 f J_0(K\mathscr{M} + \mathscr{D}HJ_0)\hat{\mathbf{V}}_1 H]$$
$$\pm \frac{1}{3}\mathscr{G}\hat{\mathbf{V}}_1 \cdot \left[H^3\hat{\mathbf{V}}_1 H - \frac{1}{2}H^3\hat{\mathbf{V}}_1(H^2 f) + \frac{9}{40}H^5\hat{\mathbf{V}}_1 f\right] = 0, \tag{25}$$

with $\hat{\mathbf{V}}_1 = (\partial_{\hat{x}}, \partial_{\hat{y}})$, and define a rescaled horizontal liquid velocity $\hat{\mathbf{U}}_I(\hat{x}, \hat{y}, \hat{t}) \equiv \mathbf{U}_{I0}/\sqrt{\text{Bo}}B$ at the interface with a straightforward extension of Eq. (B7),

$$\hat{\mathbf{U}}_I = \frac{1}{2}H^2\left[3\mathscr{D}f J_0^2\hat{\mathbf{V}}_1 H \pm 3\hat{\mathbf{V}}_1\left(\hat{\nabla}_1^2 H\right) + (3 + \mathscr{G})\hat{\mathbf{V}}_1 H - \frac{1}{2}\mathscr{G}\hat{\mathbf{V}}_1(H^2 f)\right]$$
$$+ \frac{1}{8}\mathscr{G}H^4\hat{\mathbf{V}}_1 f + 2\mathscr{M}H\hat{\mathbf{V}}_1(Hf), \tag{26}$$

where $+ (-)$ corresponds to $G < 0$ ($G > 0$); in the following the circumflex is suppressed for the rescaled variables. Equation (25) describes the evolution of the interface $H(x, y, t)$ of nonisothermal evaporating layers. In Eq. (24), the redefined dimensionless numbers have been given in terms of the original physical parameters to elucidate their physical meanings: The modified evaporation number $\mathscr{E}$ quantifies the extent of mass loss; the vapor-recoil number $\mathscr{D}$ characterizes the interfacial pressure caused by departing vapor; the modified Marangoni and Grashof numbers $\mathscr{M}$ and $\mathscr{G}$, respectively, measure the importance of thermocapillarity and buoyancy relative to hydrostatic effect. All of them depend on $\Delta\theta$ and except for $\mathscr{G}$ all include the experimental parameters of h_0, ρ, and g. Moreover, $\mathscr{E}$, $\mathscr{M}$, $\mathscr{D}$, and $\mathscr{G}$ independently depend on $\sigma_0\nu$, γ, ρ_g, and β, respectively, which could be individually controlled in experiments. Here $|\mathscr{M}| = \frac{3}{2}B_d^{-1}$, which does not depend on σ and μ, with B_d being a dynamic Bond number [7]. However, $\mathscr{M}$ may not provide a physically exact representation for thermocapillary effect as for the nonevaporating films [7,8] because the equilibrium effect of evaporation tends to suppress θ_I variation and thus the Marangoni effect [12,43] (see also the discussion of Fig. 11). When discussing the parameter magnitude, we are concerned only with the absolute values. Note, finally, that the theory just described includes the Boussinesq approximation, thus $|\text{Ra}| \ll |\text{Ga}|$ should never be violated [23]. An equivalent requirement is $|\text{Gr}| \ll |G|$ or $\frac{1}{3}|\mathscr{G}| = |\text{Gr}/G| \ll 1$ in our control parameters. As reflected from the values of $\mathscr{G}$ or Gr and G, care has been taken when choosing the parameters in our calculation.

Figure 1(b) summarizes the cases to be considered along with the organization of this study, where the signs of relevant dimensionless parameters are also indicated. We first restrict ourselves to $(1 + 1)$D cases with a sinusoidal perturbation, which are adequate to validate our numerical method and demonstrate the crucial dynamic features. Then it is necessary to investigate the $(2 + 1)$D nonlinear dynamics with more realistic random disturbances and compare the solutions with the relevant numerical or experimental results. The capacities of reproducing or anticipating various rupture patterns with large-scale drained regions, as well as the evaporation-driven LW Marangoni and LW Marangoni-Rayleigh-Bénard convection (see Sec. V), elevate the significance of the results, which would be more amenable to a direct comparison with the experiments.

B. Numerical method and validation

The strongly nonlinear partial differential equation is solved as an initial-value problem with periodic boundary conditions in the horizontal direction, which is typical for examining pattern

formation. The computational domains are $[0,\lambda)$ and $[0,l_x) \times [0,l_y)$ for the $(1+1)$D and $(2+1)$D cases, where $\lambda = \frac{\tilde{\lambda}}{h_0} = \frac{2\pi}{k}$. In the latter the diagonal length of the rectangular domain corresponds to λ and the overall wave number $k = \|\mathbf{k}\| = (k_x^2 + k_y^2)^{1/2}$ is the norm of the wave vector $\mathbf{k} = (k_x, k_y)$. The spatial derivatives are calculated with a pseudospectral method on a uniform mesh of moderate resolution, which allows simulations with high efficiency and precision, while a temporal derivative is retained. The resulting set of ordinary differential equations (ODEs) is then integrated with an adaptive time-step scheme, referred to as the method of lines. The initial condition (IC) is a small-amplitude sinusoidal or pseudorandom disturbance with $|\varepsilon_0| \ll 1$ and $|\varepsilon_1| \ll 1$,

$$H(\hat{x},0) = 1 + \varepsilon_0 \cos(2\pi \hat{x}/\lambda) \tag{27a}$$

or

$$H(\hat{\mathbf{x}},0) = 1 + m + \varepsilon_1 \mathrm{Rand}(\hat{\mathbf{x}}), \tag{27b}$$

where $\hat{\mathbf{x}} = (\hat{x}, \hat{y})$; we set $\varepsilon_0 = 0.01$ [except Fig. 2(a) and Fig. 18] and $\varepsilon_1 = -0.05$; $\mathrm{Rand}(\cdot)$ is a pseudorandom function in $(-1,1)$; m matches the initial average thickness with unity.

Considering the disjoining pressure term neglected, if the initial thickness h_0 of order 1 mm corresponds to $H = 1$, the numerical integration should be terminated once the minimum thickness $H_{\min}$ is less than a threshold of $O(10^{-4})$, corresponding to the thickness of order 100 nm. This is an indication of approaching the upper limit of a range, where the disjoining pressure due to vdW becomes dominant. Depending on the Hamaker constant A, it leads to an instantaneous rupture ($A > 0$) [31] or sets a minimum thickness ($A < 0$) acting as a lower bound, similar to the phenomena in Refs. [19,35,53]. This instant is defined as t_r. The rupture thus is never affected by the disjoining pressure and the inertial effects, since the latter is only significant just before rupture by the vdW forces [31]. Hence, the touchdown is not completely dry but a thin adsorbed layer remains [35]. Due to numerical stiffness close to rupture, the time step is reduced continually to resolve the time scale until the local solution cannot satisfy the relative spatial error. The convergence at rupture is achieved with a relative temporal error of $\frac{t_n - t_{n-1}}{t_{i=1}} = O(10^{-8})$ in the $(2+1)$D cases. Validations of our numerical method were conducted by comparing the simulation results of a LW equation in Ref. [54] with those obtained from the Newton-Kantorovich method [54] and by direct numerical simulation using the finite-element method [60] for the identical set of parameters and ICs. Both simulations for the nonevaporating layers include the effects of thermocapillarity, gravity, and surface tension. The validations provide effective tests of the capability and accuracy of reproducing the pattern formation and the robustness of resolving the rupture singularity.

In a comparison of our $(1+1)$D solution in Fig. 2(a) with that found by Krishnamoorthy *et al.* [60] using the full Navier-Stokes and energy equations [see their Fig. 2(c)], the topological structure and the appearance of fingers show good quantitative agreement, especially in the drained regions. Figure 2(b) displays the $(2+1)$D rupture pattern with remarkable similarity to that shown by Oron [54] in his Fig. 2; especially the symmetry and the circular ridges between the primary and secondary drops are fully reproduced. It is noteworthy that both the $t_r = 1988.410$ and 4737.032 found here compare quantitatively well with the $t_r = 2036.20$ and 4974.08 obtained in Refs. [54,60]. Finally, as the modeling strategies of Burelbach *et al.* [31], the values of dimensionless parameters used may not be necessarily physically realistic in order to distinguish various physics and highlight their interactions. However, these values could be satisfied by choosing the appropriate conditions, such as liquid properties, initial thickness, ambient gas, substrate temperature, and strength of gravity.

IV. LINEAR STABILITY ANALYSIS

Having derived the evolution equation in Sec. III, we now explore the time-dependent linear stability of small-amplitude perturbations, which yields an effective growth rate. Then the instabilities
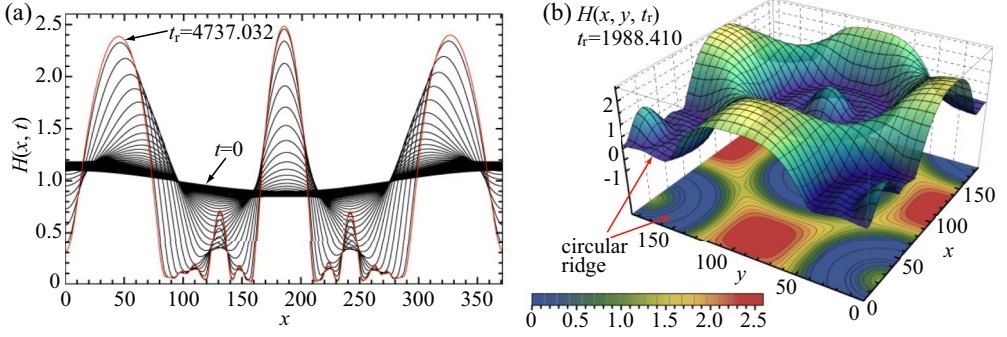
FIG. 2. Solutions obtained with $(1+1)$D and $(2+1)$D versions of Eq. (1) in Ref. [54] using the parameters (in the notation therein) Bi $= 1$, $M = 35.1$, $P = 7.02$, $G = \frac{1}{3}$, $S = 100$, and $k_m = 0.0677$. (a) Interface evolution at an interval of $100\tau_{\text{visc}}$ up to t_r with the IC $H(x,0) = 1 + 0.1\cos(\frac{1}{4}k_m x)$ and a mesh of 601 points. (b) Surface and contour plots at t_r on the domain of $l_x = l_y = 185.62$ with the IC $H(x,y,0) = 1 + \varepsilon_1[\cos(\frac{1}{2}k_m x) + \sin(\frac{1}{2}k_m x)]\cos(\frac{1}{2}k_m y)$ and an 81×81 mesh.

are examined in the quasisteady regime, justified by the fact that the basic state thins slowly compared with the growth of the most unstable perturbation and $\tau_{\text{ev}} \gg \tau_{\text{visc}}$ and τ_{th} (see Table I for the definitions of the time scales). The LSA includes various mechanisms in nonequilibrium evaporating layers and elucidates their competitions.

A. Time-dependent LSA with Bi $\to$ 0

With Bi $\to 0$, the basic state $\bar{H}(t) = -K + (1 + 2K + K^2 - 2\mathscr{E}t)^{1/2}$ vanishes at $t_e = \frac{1+2K}{2\mathscr{E}}$, as indicated in Eq. (A1a). We examine its time-dependent linear stability by perturbing the $(1+1)$D version of Eq. (25) with $H = \bar{H} + H'(x,t)$ and linearizing in H',

$$H'_t - \mathscr{E}(K + \bar{H})^{-2}H' \pm \bar{H}^3 H'_{xx} \pm \frac{1}{120}\mathscr{G}(40K^2 + 40K\bar{H} + 11\bar{H}^2)(K + \bar{H})^{-2}\bar{H}^3 H'_{xx}$$
$$\pm (K + \bar{H})^{-2}\bar{H}^2[K\mathscr{M} + \mathscr{D}(K + \bar{H})^{-1}\bar{H}]H'_{xx} + \bar{H}^3 H'_{xxxx} = 0. \qquad (28)$$

One substitutes the normal mode $H'(x,t) = H'_0 \exp(st + ikx)$ with $|H'_0| \ll 1$ into Eq. (28) to obtain the characteristic equation for growth rate s,

$$s = A_t A^{-1} = \mathscr{E}(K + \bar{H})^{-2} \pm \bar{H}^3 k^2 \pm \frac{1}{120}\mathscr{G}(40K^2 + 40K\bar{H} + 11\bar{H}^2)(K + \bar{H})^{-2}\bar{H}^3 k^2$$
$$\pm (K + \bar{H})^{-2}\bar{H}^2[K\mathscr{M} + \mathscr{D}(K + \bar{H})^{-1}\bar{H}]k^2 - \bar{H}^3 k^4, \qquad (29)$$

where $+ (-)$ is for $G < 0$ ($G > 0$) and the time-dependent normal-mode amplitude $A(t) \equiv H'_0 e^{st}$ has been introduced. By setting $K = 0$ in Eq. (29), the quasiequilibrium growth rate reads $s_{K=0} = \mathscr{E}\bar{H}^{-2} \pm (\bar{H}^3 + \mathscr{D} + \frac{11}{120}\mathscr{G}\bar{H}^3)k^2 - \bar{H}^3 k^4$. By comparing the fractions related to various mechanisms in s and $s_{K=0}$, it is found that the nonequilibrium effect ($K > 0$) reduces mass loss and vapor recoil, while it additionally brings in a destabilizing thermocapillarity. Recalling that $\mathscr{G} < 0$, it is expected that buoyancy can play a stabilizing (destabilizing) role for $G < 0$ ($G > 0$). The general solution of the ODE (29) governs the full dynamic behavior of the disturbed basic state. Setting $G < 0$, for example, its solution reads

$$A(t) = A_0 \exp\left(\int_0^t (\cdot)dt\right) = \frac{A_1}{(K + \bar{H})^{1+\alpha_1 k^2}} \exp\left\{\frac{k^2(1 - \bar{H})}{\mathscr{E}}\left[\frac{1}{4}K(1 - k^2)\sum_{n=0}^{3}\bar{H}^n\right.\right.$$
$$\left.\left. + \frac{1}{5}(1 - k^2)\sum_{n=0}^{4}\bar{H}^n - K\left(3\mathscr{D} + 2K\mathscr{M} + \frac{K^2\mathscr{D}}{(K + \bar{H})(1 + K)}\right)\right.\right.$$
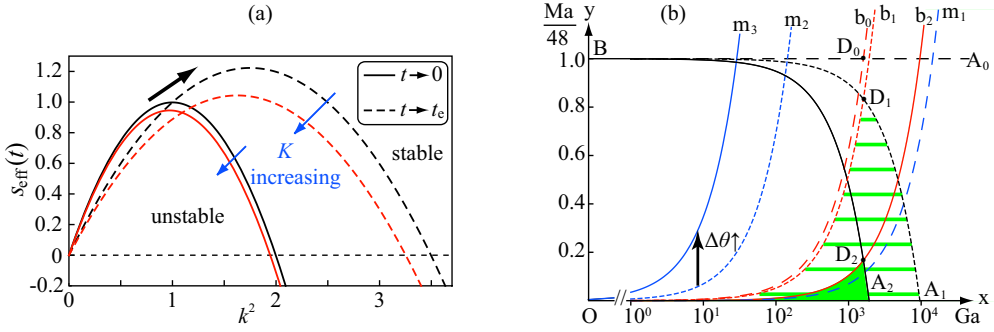
FIG. 3. Interfacial and convective stabilities of evaporating layers. (a) Plot of s_{eff} as a function of t and k for hanging layers. The dispersion curves present an increase in $s_{\text{eff},m}$ and broadening in the band of unstable modes with t. Here $\mathscr{G} = -0.023$, $\mathscr{M} = 0.29$, and $K = 8.7 \times 10^{-5}$ (upper curves) are obtained from Table II and $\mathscr{D} = 1$ is for illustration of the vapor recoil effect, feasible for a relatively small ambient pressure. The lower curves with $K = 0.02$ are appropriate for a certain experimental situation (e.g., smaller a). (b) Stability diagram of convective instabilities in sessile layers: BA_i, neutral curves without evaporation $\frac{1}{48}M_c + \frac{1}{320}R_c = 1$ [62,63]; Ob_i, neutral curves expressed in Eq. (34b) with a vapor recoil of $\mathscr{D} = -0.03$ (subscripts $i = 0,1,2$ corresponding to $\mathscr{G} = 0, -0.1, -0.5$, respectively); $Om_{j=1,2,3}$, Ma $= -\frac{1}{3}\mathscr{M}$ Ga (with $\mathscr{M} = -0.01, -1, -5$, respectively); $A_0 D_0 Ox$ and $A_{1,2} D_{1,2} O$, stability; $yBD_{1,2}b_{1,2}$, Marangoni-dominated instability; $BOD_{i=0,1,2}$, vapor-recoil-dominated instability; and $b_{1,2} D_{1,2} A_1 x$, buoyancy-dominated instability. Logarithmic scale is used for the abscissa for large values of Ga (e.g., ground conditions). All the curves are straight on a linear scale.

$$+ \frac{1}{2}(1 + 2K + \bar{H})[\alpha_2(K + \bar{H}) + \alpha_3]$$

$$+ \frac{1}{600}\mathscr{G}\left(\frac{31}{4}K - 11\bar{H}\right)(1 - \bar{H})(1 + 2K + \bar{H})^2 + \alpha_4\bigg]\bigg\}, \tag{30}$$

where the upper limit of the integral $t < t_e$, $(\cdot)$ denotes the right-hand side of Eq. (29), A_0 and A_1 are integration constants, $\alpha_1 = (3\mathscr{D} + K\mathscr{M} - \frac{11}{120}K^3\mathscr{G})K^2\mathscr{E}^{-1}$, $\alpha_2 = \frac{1}{450}\mathscr{G}(33 + 66K + 8K^2)$, $\alpha_3 = \mathscr{D} + K\mathscr{M} - \frac{1}{24}K\mathscr{G}(3 + 6K + K^2)$, and $\alpha_4 = \frac{1}{1800}\mathscr{G}(33 + 132K + 148K^2 + 32K^3 + 208K^4)$. The term $(K + \bar{H})^{-1-\alpha_1 k^2}$, resulting from mass loss, gives just an algebraic variation and does not affect the exponential stability. With the exponent in Eq. (30) divided by t to exclude the algebraic contribution of mass loss, a time-dependent effective growth rate can be defined [31,36], $s_{\text{eff}}(t) = \frac{2k^2[\cdots]}{1 + 2K + \bar{H}}$, in which $\mathscr{E}$ is absent and $[\cdots]$ represents the polynomial in the square brackets of Eq. (30). A positive value of s_{eff} corresponds to linear instability. The maximum value $s_{\text{eff},m}$ occurs at $k_m = \frac{k_c}{\sqrt{2}}$. There are two limiting cases,

$$s_{\text{eff}} \to k^2\left\{1 - k^2 + \alpha_2(1 + K) + \alpha_3 + \frac{\alpha_4}{1 + K} - \frac{K}{1 + K}\left[3\mathscr{D} + 2K\mathscr{M} + \frac{K^2\mathscr{D}}{(1 + K)^2}\right]\right\} \quad \text{as } t \to 0,$$

$$s_{\text{eff}} \to \frac{k^2}{1 + 2K}\left[\left(\frac{2}{5} + \frac{1}{2}K\right)(1 - k^2) - 2K\left(3\mathscr{D} + 2K\mathscr{M} + \frac{K\mathscr{D}}{1 + K}\right) + \frac{31}{1200}\mathscr{G}K(1 + 2K)^2\right.$$

$$\left. + (1 + 2K)(\alpha_2 K + \alpha_3) + 2\alpha_4\right] \quad \text{as } t \to t_e,$$

and the cutoff wave number $k_c(t)$ corresponds to $s_{\text{eff}}(t) = 0$. As shown in Fig. 3(a), both the unstable interval and $s_{\text{eff},m}$ increase with time. This implies that interface instability is enhanced by vapor thrust, which competes with the stabilization of surface tension to select a wavelength. Its destabilizing mechanism makes sense physically: A mechanical perturbation at the surface will be reinforced as temperature gradients at a trough become greater. The local evaporation rate and thus momentum

flux associated with vapor recoil become stronger since the former is proportional to heat flux at the interface. With the heat flux increasing, a trough becomes deeper. Therefore, it suggests a physical possibility of finite-time rupture, independent of thermocapillarity and the direction of gravity [32]. This argument is true in both quasiequilibrium and nonequilibrium cases, as demonstrated by the subsequent nonlinear simulation. Moreover, the intrinsic stabilization of nonequilibrium can be identified by comparing the two pairs of curves with increasing K and the fixed $\mathscr{M}$.

The most unstable perturbation is expected to grow much faster than the basic-state vanishing that one could freeze it at $\bar{H}(0) = 1$ [30,36]. Thus Eq. (29) becomes

$$s_s = \mathscr{E}(1 + K)^{-2} \pm \tfrac{1}{120}\mathscr{G}(11 + 40K + 40K^2)(1 + K)^{-2}k^2$$
$$\pm [1 + K\mathscr{M}(1 + K)^{-2} + \mathscr{D}(1 + K)^{-3}]k^2 - k^4, \tag{31}$$

with the subscript s for quasisteady theory, which gives a factitious instability due to the nature of thinning, i.e., $s_s = \mathscr{E}(1 + K)^{-2}$ for an undisturbed interface ($k = 0$). Letting $\mathscr{E} = 0$ exclude the mass-loss contribution, one finds

$$k_{c,s}^2 = \pm[1 + \mathscr{D}(1 + K)^{-3} + K\mathscr{M}(1 + K)^{-2} + \tfrac{1}{120}\mathscr{G}(11 + 40K + 40K^2)(1 + K)^{-2}]. \tag{32}$$

To compare with quasisteady results under quasiequilibrium, it follows that $s_{K=0,s} = \pm(1 + \mathscr{D} + \tfrac{11}{120}\mathscr{G})k^2 - k^4$ and $k_{K=0,c,s}^2 = \pm(1 + \mathscr{D} + \tfrac{11}{120}\mathscr{G})$ with $\bar{H} = 1$ and $\mathscr{E} = 0$. The comparison of $k_{c,s}$ and $k_{K=0,c,s}$ reflects again the fact that nonequilibrium weakens vapor recoil but induces thermocapillarity. For $K = o(1)$ Eq. (31) can be expanded in a power series at leading order,

$$s_{s,0} = \mathscr{E}(1 - 2K) \pm [1 + K\mathscr{M} + \mathscr{D}(1 - 3K) + \tfrac{1}{120}\mathscr{G}(11 + 18K)]k^2 - k^4. \tag{33}$$

With $\mathscr{E} = 0$, it recovers the quasiequilibrium growth rate $s_{K=0,s}$, if $\mathscr{M} - 3\mathscr{D} + \tfrac{3}{20}\mathscr{G} = 0$ is satisfied. For small K, the quasisteady linear theory thus predicts a critical value for $\mathscr{M}$ between quasiequilibrium and nonequilibrium states,

$$\mathscr{M}_{c,s}^{\pm} = 3\big(\mathscr{D} - \tfrac{1}{20}\mathscr{G}\big) \tag{34a}$$

or

$$\tfrac{1}{48}M_c + \tfrac{1}{320}R_c = \tfrac{1}{16}\mathrm{Pr}E^2 D^{-1} = \tfrac{1}{48}\mathrm{Ga}(-\mathscr{D}) \quad \text{for } G > 0, \tag{34b}$$

with the superscript $+ (-)$ for positive (negative) gravity in Eq. (34a). Furthermore, for given $K, k, \mathscr{D}$, and $\mathscr{G}$ with different $\mathscr{M}$, the quasisteady analysis shows that here s_{eff} can be increased or decreased relative to the quasiequilibrium s_{eff}, depending on the relative magnitude of the parameters, such as K and $\mathscr{M}$. We therefore predict, and indeed will find, that a critical $\mathscr{M}$ also exists in the nonlinear regimes (see Sec. V C).

The equivalent form in Eq. (34b) is reminiscent of the classical relation at threshold of LW convective instability ($k \to 0$) in a nonevaporating layer heated from below with a weakly deformable free surface at $\mathrm{Bi} \to 0$ [62,63] when $\tfrac{1}{16}\tfrac{\mathrm{Pr}E^2}{D} = 1$, in which the critical Ma, with Ra $= 0$, $M_c^0 = 48$ [6] [Marangoni convection, region yBA_0 in Fig. 3(b)] and the critical Ra, with Ma $= 0$, $R_c^0 = 320$ [64] (RB convection, lines $A_{1,2}x$). In Fig. 3(b), the neutral stability loci are plotted on the (Ga,Ma) plane. In classical stability diagram [4], for a given $\mathscr{M}$, convection does not start until the intersection between BA_i and Om_j [here $i = 0,1,2$ and $j = 1,2,3$; see the caption of Fig. 3(b)]. In the presence of vapor recoil, in contrast, convection can be initiated for small Ma and Ga unless $\mathscr{M}$ is so low that the point ($\tfrac{1}{48}$Ma,Ga), corresponding to a certain $\Delta\theta$ and h_0, falls within the stable zones $A_{1,2}D_{1,2}O$ (e.g., Om_1 through green triangles), where an evaporating layer is motionless. Physically, heating a given fluid with a fixed h_0 means rotating the Om_j line, Ma $= \tfrac{-1}{3}\mathscr{M}$Ga, counterclockwise as $\mathscr{M} \propto \Delta\theta$ (see $Om_2 \Rightarrow Om_3$), thus a point with a constant value of h_0 translates upward and the layer tends to be destabilized by the Marangoni effect. Furthermore, as $\Delta\theta$ increases the intersection

D_i $(-48\mathscr{D}^{-1}, 1 - \frac{1}{320}\mathrm{Ra})$ of BA_i and Ob_i approaches the origin O. It reflects the destabilizing roles of vapor recoil and buoyancy. For a large value of h_0, the instability reduces to the RB convection, while the vapor recoil and Marangoni effects dominate the instability for small h_0. Finally, the LW deformation, considered as a non-Boussinesq effect, and flow fields will be studied later in the nonlinear simulation (Secs. V and VI).

B. General LSA with Bi > 0: Frozen-time approach

Similarly, we perform the LSA by superimposing a small perturbation on the basic-state solution (A1a) $H = \bar{H}(T) + H'(X, T)$, where $H' = H_0' \exp(sT + ikX) = A(T)e^{ikX}$ with the normal-mode amplitude $A(T) \equiv H_0'e^{sT}$ and $|A| \ll \bar{H}$. Substituting the expression into Eq. (21) and linearizing in H', we obtain an ODE $s = A_T A^{-1} = \Pi_{\mathrm{ev}}(T) + \Pi_{\mathrm{eff}}(T)$, where the two real terms are given by $\Pi_{\mathrm{ev}}(T) = Ef(\bar{H})J_0(\bar{H})$ and

$$\Pi_{\mathrm{eff}}(T) = \big(E^2 D^{-1}(1 + \mathrm{Bi}K)[\bar{H}J_0(\bar{H})]^3 + K\,\mathrm{Ma}\,\mathrm{Pr}^{-1}(1 + \mathrm{Bi}K)[\bar{H}J_0(\bar{H})]^2 - \tfrac{1}{3}G\bar{H}^3$$
$$+ \tfrac{1}{120}\mathrm{Gr}\bar{H}^3\big\{11 + K[29K + 18(1 + \mathrm{Bi}K)\bar{H}]J_0^2(\bar{H})\big\} - k^2\Sigma_0\bar{H}^3\big)k^2.$$

To avoid a complicated expression for the dynamics of the disturbed interface, e.g., Eq. (30), it is equivalent to define $\Pi_{\mathrm{eff}}(T)$ as a time-dependent effective growth rate. The definition not only eliminates a spurious destabilization emerging from mass loss [31], which is associated with $\Pi_{\mathrm{ev}}(T)$ and gives an algebraic variation in $A(T)$, but also is convenient in interpreting the interactions of various mechanisms. The stability condition is $\Pi_{\mathrm{eff}} < 0$.

The successive terms in Π_{eff} embody the destabilizing effects of vapor thrust and thermocapillarity, the stabilizing (destabilizing) mechanism of hydrostatic pressure with destabilizing (stabilizing) buoyancy for $G, \mathrm{Gr} > 0$ ($G, \mathrm{Gr} < 0$) [cf. Fig. 1(b)], and the stabilization due to surface tension. With $\Pi_{\mathrm{eff}} = 0$ the time-dependent cutoff wave number is found to be

$$k_c(T) = \big\{\Sigma_0^{-1}\big[E^2 D^{-1}f(\bar{H})J_0^2(\bar{H}) + K\,\mathrm{Ma}\,\mathrm{Pr}^{-1}\bar{H}^{-1}f(\bar{H})J_0(\bar{H}) - \tfrac{1}{3}G + \tfrac{11}{120}\mathrm{Gr}$$
$$+ \tfrac{3}{20}\mathrm{Gr}K\bar{H}f(\bar{H})J_0(\bar{H}) + \tfrac{29}{120}\mathrm{Gr}K^2 J_0^2(\bar{H})\big]\big\}^{1/2}. \tag{35}$$

The interval of unstable modes is $0 < k < k_c$ provided the expression in square brackets in Eq. (35) is positive. The maximum growth rate $\Pi_{\mathrm{eff},m}$ corresponds to $k_m = k_c/\sqrt{2}$. For the nonvolatile case ($K \to \infty$ and $E = 0$) with $\bar{H} = 1$ and $G > 0$, when the buoyancy and capillarity are negligible, it recovers a stability condition in Ref. [60], characterizing the competition between the stabilizing gravity and destabilizing thermocapillarity,

$$G > 3\,\mathrm{Ma}\,\mathrm{Bi}\,\mathrm{Pr}^{-1}(1 + \mathrm{Bi})^{-2}, \tag{36}$$

where the Marangoni effect obtains the maximum with $\mathrm{Bi} = 1$.

Figure 4(a) illustrates k_c as a function of $\bar{H}$ for the representative values of Ma in the absence or presence of positive or negative gravity. These values of parameters are chosen to distinguish the influences of thermocapillarity and gravity. The unstable spectrum is located below the corresponding curve. The dotted line displays the behavior of k_c for a nonvolatile zero-gravity film subject to the Marangoni effect and surface tension only, according with that presented in Ref. [41]. For $g > 0$ and smaller Ma, above a certain critical thickness the basic state is stable to a LW disturbance with the stabilizations of hydrostatic pressure and surface tension and the critical thickness decreases with a decrease in Ma. This property is in agreement with a recent result of Kanatani [65], who took into account the diffusion and convection of vapor with a concentration boundary layer model. With $g \leqslant 0$ the quasisteady uniform layer is always unstable to infinitesimal perturbations of the normal-mode form even for Ma $= 0$, that is, the wave number at onset is zero. A comparison between the four curves in the case of $G = 0$, $G > 0$, or $G < 0$ in the increasing sequence of Ma demonstrates its destabilizing effect, which becomes more significant as the layer thins, reflected by the rapid
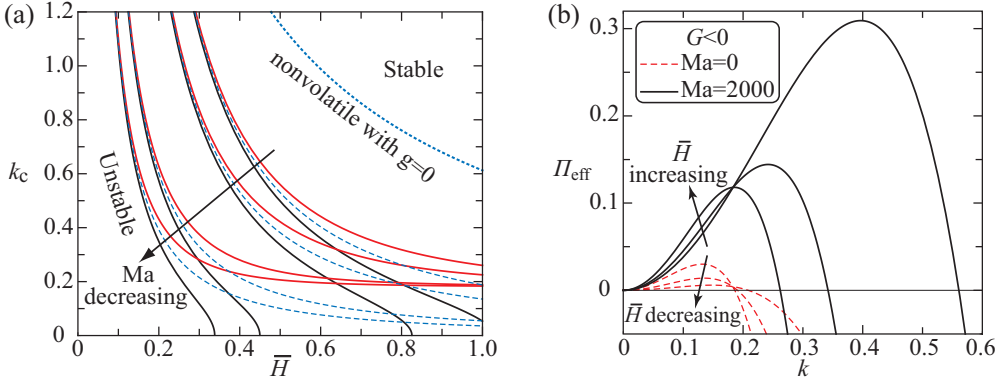
FIG. 4. Interactions of thermocapillarity and gravity with $\Sigma_0 = 100$ and $K = 0.003$. (a) Plot of k_c as a function of $\bar{H}$ represented by four groups of curves with $\mathrm{Ma} = 2000, 1000, 100, 0$ and $\mathrm{Bi} = 1$. The solid lines show $|G| = 10$ and $|\mathrm{Gr}| = 1$, the lower (upper) family for $G > 0$ ($G < 0$); the dashed lines show $G = 0$; and the dotted line shows the nonvolatile weightless case with $K \to \infty$, $E = G = 0$, $\mathrm{Ma} = 1$, $\Sigma_0 = 1/3$, and $\mathrm{Pr} = 2$ to recover the dotted line in Fig. 2 of Ref. [41]. (b) Dispersion curves in the case of RTI for $G = -10$, $\mathrm{Bi} = \mathrm{Gr} = 0$, and $\bar{H} = 1$, $3/4$, and $1/2$. The other parameters are taken from Table II in Appendix A.

expansion of the unstable spectrum. The (de)stabilization of gravity is obvious in a thicker layer, as suggested by the merging of the curves in each group as $\bar{H}$ decreases, while the destabilizing effects of vapor recoil and thermocapillarity prevail. This point is consistent with the subsequent discussion of the nonlinear evolution.

Considering a frozen basic state, the quasisteady behaviors of Π_{eff} are plotted in Figs. 4(b) and 5 as a function of k with the fixed values of $|G| = 10$ and $\Sigma_0 = 100$ for demonstration. In Fig. 4(b), the dynamic characteristics of thermocapillarity on a Rayleigh-Taylor unstable layer are revealed by comparing the Π_{eff} behaviors with $\mathrm{Ma} = 0$ and 2000 for the three pairs of dispersion curves in the decreasing sequence of $\bar{H}$: decaying $\Pi_{\mathrm{eff},m}$ and slightly increasing k_m and k_c without thermocapillarity, and rapidly increasing $\Pi_{\mathrm{eff},m}$, k_m, and k_c in the presence of thermocapillarity. It demonstrates that thermocapillarity exerts more significant destabilization as the layer thins by accelerating the disturbance growth and extending the unstable spectrum.

The physical situation considered next is an evaporating layer heated from the substrate subject to positive gravity as $G, \mathrm{Gr} > 0$ in Fig. 1(b). Figure 5 reveals the influences of ambient cooling and buoyancy by comparing the differences between solid and dashed curves in each pair. To illustrate that E exerts a considerable influence on linear stability, Figs. 5(a) and 5(b) plot Π_{eff} for $E = 0.03, 0.06, 0.09$ with $K = 0.003$, corresponding to three pairs of dispersion curves with increasing k_c and $\Pi_{\mathrm{eff},m}$. The results suggest that the stabilization of the cooling effect becomes more evident with increasing E, while the destabilization of buoyancy remains minor. Based on the Boussinesq
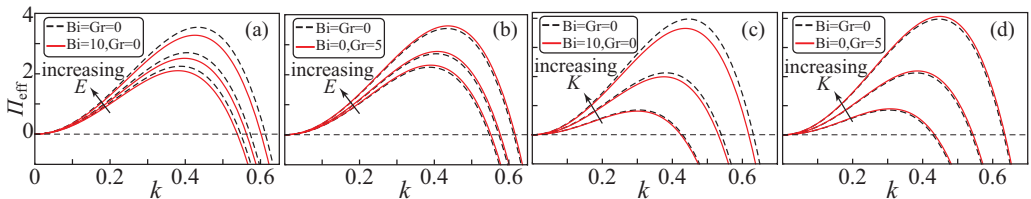

FIG. 5. Three pairs of dispersion curves with $\bar{H}(0) = 1$ and $G = 10$ for $E = 0.03, 0.06, 0.09$ with $K = 0.003$ or for $K = 0.002, 0.003, 0.004$; the other parameters are taken from Table II. Influences of (a) and (c) ambient cooling and (b) and (d) buoyancy are shown.
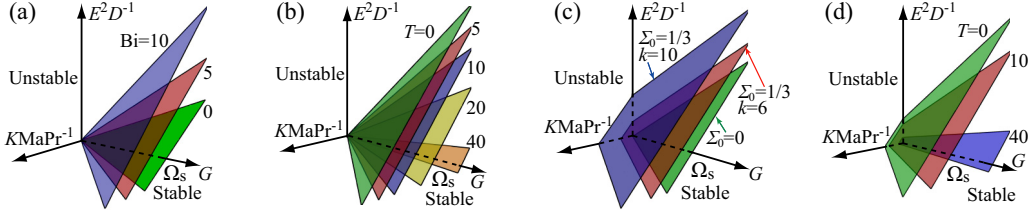
FIG. 6. Stability diagram with $K = 0.06$, $Ra = 0$, and $E = 0.011$ for $G > 0$: (a) $\bar{H} = 1$ and $\Sigma_0 = 0$ with different Bi, (b) as layer thins with Bi $= 1$ and $\Sigma_0 = 0$ ($T_e = 53.636$), (c) $\bar{H} = 1$ and Bi $= 5$ with different Σ_0 and k, and (d) as layer thins with Bi $= 5$, $k = 6$, and $\Sigma_0 = 1/3$ ($T_e = 64.545$).

approximation, $\beta \Delta \theta \ll 1$, hence Gr $\ll G$. The value of Gr is chosen to highlight the buoyancy effect; nevertheless, it just slightly broadens the unstable spectrum and marginally increases $\Pi_{\text{eff},m}$, as can be seen in Fig. 5(b). Another quantity strongly affecting the stability is K. Three pairs of dispersion curves are plotted for $K = 0.002, 0.003, 0.004$ in Figs. 5(c) and 5(d). Figure 5(c) implies that the cooling effect can exert a significant stabilization when evaporation deviates far enough from quasiequilibrium. The destabilizing effect of buoyancy is found to be relatively weak again from Fig. 5(d). We thus expect that buoyancy exerts a weak destabilization on the interfacial stability with $G > 0$. Within the parameter range, Π_{eff} is quite sensitive to K as the induced thermocapillarity dominates over its intrinsic stabilization. Figures 5(a) and 5(c) show that the enhancement of ambient cooling narrows down the range of unstable modes and decreases $\Pi_{\text{eff},m}$; it thus is expected to decelerate the rupture, as indeed found later in the nonlinear regime. The stabilization of ambient cooling makes sense physically because it acts as a dissipative mechanism, competing for energy to be consumed by evaporation. With larger Bi (smaller thermal resistance in ambient cooling), it is more difficult for temperature perturbation to be set up and the interface deformation induced by the Marangoni effect tends to be damped.

Figure 6 displays the interactions among vapor thrust $\frac{E^2}{D}$, thermocapillarity $\frac{K \text{Ma}}{\text{Pr}}$, and gravity ($G > 0$) on the quasisteady stability of the evaporating layer for $K = 0.06$ and $\bar{R} = 0$. It is stable ($\Pi_{\text{eff}} < 0$) within a stability space Ω_s bounded by the coordinate planes and a neutral surface. In Fig. 6(a), with increasing Bi, Ω_s expands and the projection of the intersection between the neutral surface and constant-G plane onto the ($\frac{E^2}{D}, \frac{K \text{Ma}}{\text{Pr}}$) plane yields a segment with increasing slope, which means that reinforcement of the ambient cooling leads to a more stable interface by weakening thermocapillarity and vapor recoil. When $\frac{E^2}{D} = \frac{K \text{Ma}}{\text{Pr}} = 0$, we are restricted to the G axis where a nonvolatile layer behaves stably [see Eq. (36)]. With $\frac{E^2}{D} > 0$ and $\frac{K \text{Ma}}{\text{Pr}} = 0$ one moves along a straight line parallel to the G axis; instability is present with small G originating from vapor recoil and then stabilized by the hydrostatic pressure. Similarly, with $\frac{K \text{Ma}}{\text{Pr}} > 0$ and $\frac{E^2}{D} = 0$ along a line parallel to the G axis, $\Pi_{\text{eff}} > 0$ results from thermocapillary instability for small G and then it becomes negative due to the stabilization of gravity. As illustrated in Fig. 6(b), Ω_s shrinks as the layer thins with T since vapor thrust and thermocapillarity become dominant. Figure 6(c) shows that Ω_s expands in the presence of surface tension and further with increasing k because capillarity stabilizes disturbances of shorter wave. When $G = 0$ and $\Sigma_0 \neq 0$, $\frac{E^2}{D}$ and $\frac{K \text{Ma}}{\text{Pr}}$ reach the upper limits for instability at the intersection of the ($\frac{E^2}{D}, \frac{K \text{Ma}}{\text{Pr}}$) plane and a neutral surface and destabilizations of vapor thrust and thermocapillarity are inhibited for relatively small k. In Fig. 6(d), the intersection between ($\frac{E^2}{D}, \frac{K \text{Ma}}{\text{Pr}}$) and neutral planes approaches the origin with time, which means the stabilization of surface tension becomes less effective. The slope of the intersection between the neutral surface and the plane of ($\frac{E^2}{D}, G$) or ($\frac{K \text{Ma}}{\text{Pr}}, G$) decreases as Ω_s shrinks. That is, the stabilization of gravity weakens and rupture instability is dominated by vapor recoil and thermocapillarity with time. The predictions coincide with our nonlinear simulations reported below.
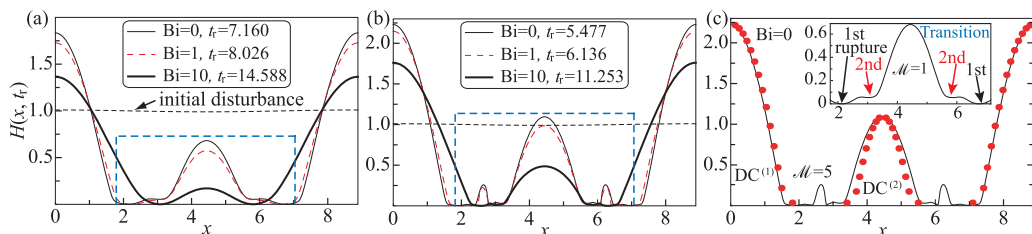
FIG. 7. Rupture patterns of case I evaporating layers subject to RTI for $\lambda = 2\sqrt{2}\pi$, $K = 0.1$, $\mathscr{E} = 0.05$, $\mathscr{D} = 1$, $\mathscr{G} = -0.2$, and different Bi with a mesh of 201 points. (a) $\mathscr{M} = 1$. (b) $\mathscr{M} = 5$. (c) Lines represent numerical solutions of Eq. (25) and circles show the corresponding DCs with Eq. (44). The inset shows a close-up of the window of (a) illustrating the transition to (b) (see the text in Sec. VI B). Here a large value of Bi could be suitable with these considerations: (i) It could be achieved in an experiment where a liquid layer of low k_{th} (e.g., HFE-7300) is surrounded by a thin gas layer with a high $k_{\text{th},g}$ (e.g., helium, similar to the experiment of VanHook *et al.* [8]), (ii) evaporation can give an explanation through a thermal dissipation mechanism along interface as if the gas had a large $k_{\text{th},g}$ [12], and (iii) a large Bi could be taken in the parameter study [6].

V. TIME-DEPENDENT SIMULATIONS: AMBIENT COOLING, FLOW FIELD, AND (2 + 1)D PATTERN FORMATION

The linear stability analysis in the above discussion, however, is valid for the predictions of initial and quasisteady growth rates of infinitesimal perturbations. To follow the surface transition from a small disturbance to rupture in nonlinear regimes, Eq. (25) will be solved numerically in three cases: case I for weak mass loss of $\mathscr{E} = O(10^{-2})$ and strong vapor thrust of $\mathscr{D} = O(1)$, case II for moderate mass loss of $\mathscr{E} = 0.1$ and strong vapor thrust, and case III for moderate evaporation at $\mathscr{E} = |\mathscr{D}| = 0.1$. In the four sections below for the negative (Sec. V A) and positive (Sec. V B) gravity cases, we first report simpler solutions of the $(1 + 1)$D version of Eq. (25) on a small domain $[0, \lambda_m]$ with the IC (27a) for case I to illustrate the stabilizing effect of ambient cooling and the flow-field evolution with the contribution of buoyancy, where $\lambda_m = 2\sqrt{2}\pi$ is the most unstable wavelength for nonvolatile isothermal layers subject to RTI from the linear theory. Next, representative $(2 + 1)$D patterns on an extended domain for case III are presented using the random perturbation shown in Eq. (27b) in view of the dependence of the $(2 + 1)$D dynamics on the form of IC [45,54]. In Secs. V C and V D, the influences of gravity and buoyancy are further demonstrated with a rescaled pressure and an average Nusselt number, respectively.

A. Evaporating layer subject to negative gravity (RTI)

Figures 7(a) and 7(b) show the rupture patterns for RTI by changing $\mathscr{M}$ and Bi. With increasing Bi, the drained region shrinks, the heights of droplets are reduced, the capillary ridges are suppressed, and rupture is retarded. This demonstrates the stabilization of ambient cooling in the fully nonlinear regime that coincides with our linear analysis. A physical explanation for this stabilization has been ascertained from Figs. 5(a) and 5(c). Also, as can be seen from Eq. (25), as Bi increases the effects of mass loss, vapor recoil, and thermocapillarity should be reduced since the common multiplicative term J_0 is a decreasing function of Bi. The mitigation for Marangoni effect is in agreement with the thermal dissipation mechanism presented in [12], which acts as an effective heat conductivity of the gas. In addition, after the (first) rupture the solutions have compact supports (i.e., droplets with zero contact angle), as discussed for LW Marangoni flow without evaporation [49,50]. Furthermore, the transition between Figs. 7(a) and 7(b) can be explained with the properties of a DC [49], in Sec. VI B.

To quantify the flow field with the solution of the canonical equation (25), we define a rescaled stream function $\Psi(x, z, t) \equiv \text{Bo}^{1/2} E^{-1} \psi$ according to Eq. (B6) in the rescaled variables [Eq. (23) with $z = Z$] and the redefined dimensionless numbers [Eq. (24)]

$$\Psi = \pm \hat{\Lambda}\left(\tfrac{1}{6}z^3 - \tfrac{1}{2}Hz^2\right) \pm \mathscr{E}^{-1}H_x f J_0 z^2\left[\tfrac{1}{12}\mathscr{G}(1 + \text{Bi}K)\left(\tfrac{1}{10}z^3 - H^3\right) + \mathscr{M}K\right], \quad (37)$$
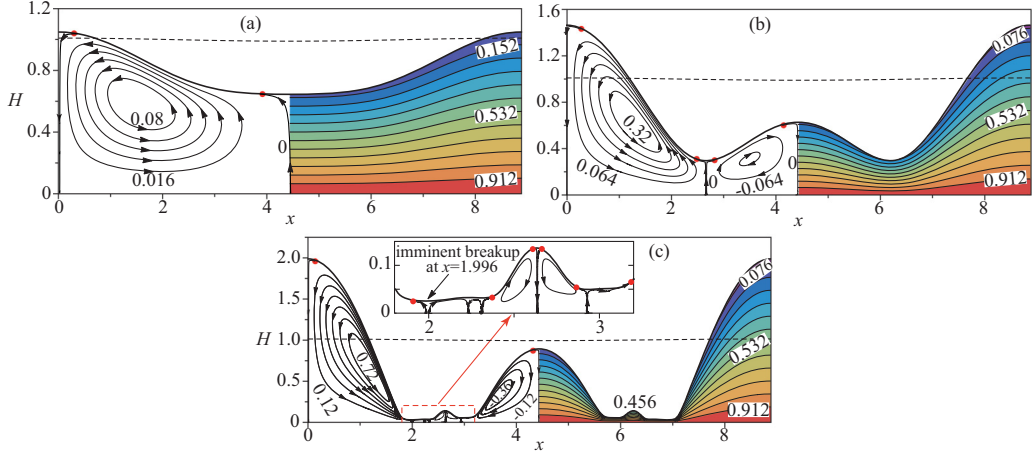
FIG. 8. Streamlines and isotherms of the case I evaporating layer subject to RTI at three representative moments, calculated for $\lambda = 2\sqrt{2}\pi$, $K = 0.1$, $\mathscr{E} = 0.05$, $\mathscr{D} = 1$, $\mathscr{M} = 5$, $\mathscr{G} = -0.2$, and Bi $= 1$ with a mesh of 201 points. Contours are separated by intervals of $\Delta\Psi$ and $\Delta\Theta = 0.076$. (a) Initial stage of valley formation ($\Delta\Psi = 0.016$) at $t = 4.2$. (b) Emergence of a secondary droplet ($\Delta\Psi = 0.064$) at $t = 5.6$. (c) Formation of drained regions just before rupture ($\Delta\Psi = 0.12$) at $t = 6.08$. The inset shows an enlarged intervening film. The initial disturbance is shown by the black dashed line. The red dots highlight intersections where streamlines $\Psi = 0$ cross the free surface, although some of them seem to be tangential to the interface owing to the influences of negative gravity on interfacial velocity and its slope under weak mass loss.

where $\hat{\Lambda} = \mathrm{Bo}^{1/2} E^{-1} \Lambda = -\mathscr{E}^{-1}[3\mathscr{D} H_x f J_0^2 \pm 3 H_{xxx} + (3 + \mathscr{G}) H_x - \frac{1}{2}\mathscr{G}(H^2 f)_x]$. As illustrated in Fig. 8, the transient interface, streamlines, and isotherms are calculated at three representative moments. The convective cells are encompassed by the substrate $z = 0$, the interface $z = H$, and the dividing streamlines $\Psi = 0$ which cross the free surface. The number of cells is double that of the interfacial minima, e.g., with six minima at $t = 6.08$, twelve cells are accommodated. The streamlines also indicate the occurrence of recirculation inside the bulges. As shown in Fig. 8(a), the liquid descends (note that $G < 0$) at the center of the interval, where the evaporation rate is larger and then a part of interfacial fluid crosses the surface due to mass loss and the remainder is drawn toward the interior by the Marangoni effect and pressure gradient; while rising it loses kinetic energy by acting against gravity combined with buoyancy (cf. discussion for Fig. 13) and travels quickly to the center along an isotherm. The isotherms show that temperature increases vertically from the interface to the bottom, while they vary slowly on a lateral scale, arising from the lubrication approximation and manifesting the diffusion-dominant heat transfer. Moreover, the temperature gradients of $\nabla_s \theta_I$ and $\nabla\theta$ are larger where the layer is thinner. The thermocapillary convection should be the dominant energy transport mode near the troughs where the Marangoni stresses and mass loss tend to the localized maxima. This is true in the positive gravity case as well.

Interesting phenomena can be observed from the flow-field evolution. During the early stage in Figs. 8(a) and 8(b), a shallow valley and two large vortices are developed, which are squeezed as the formations of a middle bulge and two secondary vortices. The local velocity increases because of the Marangoni stresses ($\nabla_s \sigma = -\gamma \nabla_s \theta_I$) near the lateral sides of the valley, which increase as the valley deepens, especially nearby the troughs [see the isotherms in Figs. 8(b) and 8(c)]. The deformation of the secondary vortex is very similar to that of the previous larger one, which allows a self-affine interface (Sec. VI B). The inset of Fig. 8(c) shows an enlarged part of the film covering a drained region, where a tertiary and an additional bulge are perceptible. The streamlines are asymmetric there due to the distinct pressures on either of their sides. The flow in the intervening film is sufficiently slow since a thinner film has a higher viscous resistance. Finally, $\nabla_s \theta_I$ and thus the Marangoni convection vanishes in the film just before rupture.
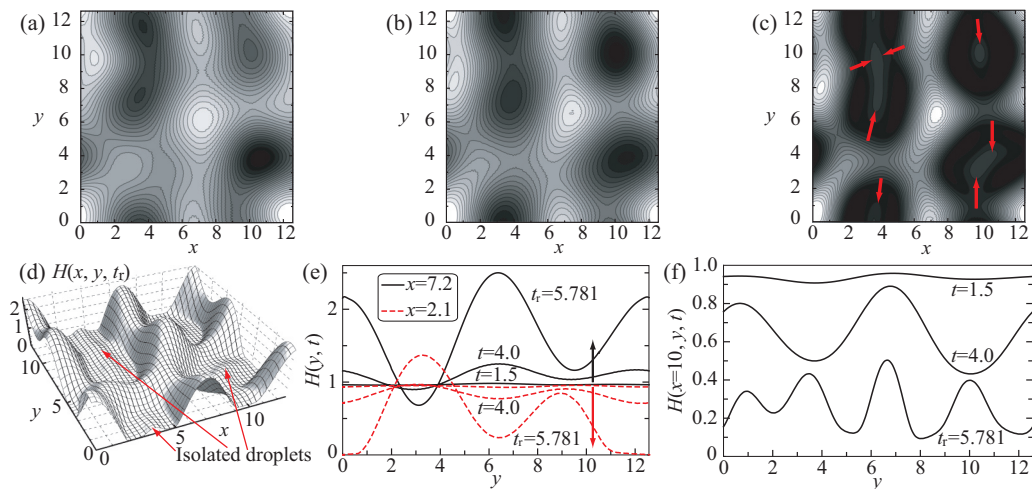
FIG. 9. Evolution of the case III evaporating layer subject to RTI for $K = 1$, $\mathscr{E} = 0.1$, $\mathscr{D} = 0.1$, $\mathscr{M} = 5$, $\mathscr{G} = -0.1$, and Bi $= 1$. The side length of the periodic domain is 4π. A uniform 151×151 mesh is employed. The number of semidiscrete ODEs to be integrated at each step is 22 500. Successive snapshots of the interface contour with the minimum and maximum elevations ($H_{\min}$ and $H_{\max}$) are shown at (a) $t = 1.5$ (0.9039 and 0.9885), (b) $t = 4$ (0.4312 and 1.3231), and (c) $t_r = 5.781$ (5.9019×10^{-5} and 2.5040). Red arrows denote the orientation of the breakup of annular dry patches. (d) Surface plot at t_r. Also shown is the evolution of representative profiles for (e) $x = 2.1$ and 7.2 and (f) $x = 10$.

Afterward, Eq. (25) is solved on a square periodic domain $[0,l] \times [0,l]$ with the IC (27b) and $l = 4\pi$, whose diagonal fits the disturbance of $\lambda = 2\lambda_m$. The surface is presented in the form of grayscale contour, where the bright (dark) shades correspond to thick (thin) regions. Note that each contour has its own brightness scale, thus different images cannot be compared directly. A representative case III evolution subject to RTI, shown in Fig. 9, results in an irregular morphology of a polygonal network of ridges spaced by large-scale drained regions at the moment of rupture. Its evolution undergoes three stages (movie 1 in the Supplemental Material [66]): (i) self-organization of random perturbation and emergence of bumps and dimples driven by initial linear instability, (ii) broadening and/or deepening of the depressions at some regions while elevating the humps at others [Figs. 9(a), 9(b), 9(e)], and (iii) further development (broadening, deepening, or coalescing) of drained regions along with the emergence of increasingly small structures until rupture [Figs. 9(c), 9(d), 9(f)]. It is found that in general rupture occurs in the vicinity of higher ridges or drops, where the cracked annular dry patches emerge [Figs. 9(c) and 9(d)]. It can be ascribed partly to the surface gradients and thus Marangoni stresses being greater there and partly to the stronger local vapor recoil. Another phenomenon that appears near rupture is the formation of isolated droplets, corresponding to a tertiary structure in the $(1 + 1)$D case and similar to the localized patterns in [67], which are trapped within the drained regions and lead to the breakup of annular dry patches.

The surface patterns in Figs. 9(c) and 9(d) are analogous to a solution obtained by Bestehorn and Merkt [28] in their Fig. 6(b) from an extended Cahn-Hilliard (CH) equation, which has similar dynamics to their Eq. (9). Both patterns appear as a set of roughly parallel striations oriented along the domain side. A difference is recognizable, but this should not be of surprise because their result was found according to a simplified model with a generalized functional involving the Ginzburg-Landau free energy and the potential energy of a point charge (see Appendix C). Our liquid layer cannot sustain a continuous stationary pattern due mainly to the opposite heating and the inclusion of vapor recoil and thermocapillarity, which were neglected in Ref. [28].
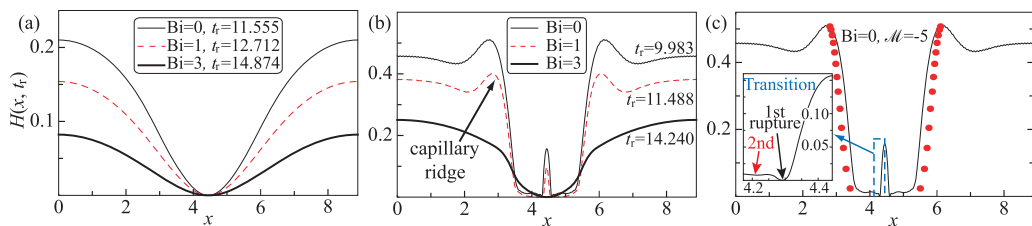
FIG. 10. Rupture patterns of the case I evaporating layers lying on substrates for $\lambda = 2\sqrt{2}\pi$, $K = 0.1$, $\mathscr{E} = 0.05$, $\mathscr{D} = -1$, $\mathscr{G} = -0.2$, and different Bi with a mesh of 201 points. (a) $\mathscr{M} = -1$. (b) $\mathscr{M} = -5$. (c) $\mathscr{M} = -5$, with lines representing numerical solution of Eq. (25) and circles showing the DC with Eq. (44). The inset shows a close-up of the window illustrating the next rupture (see the text in Sec. VI B).

B. Evaporating layer subject to positive gravity

Switching to $G > 0$ for a comparison with the just discussed case of $G < 0$, we show in Figs. 10(a) and 10(b) the influences of cooling by overlaying gas on a rupture pattern for two values of $\mathscr{M}$. It is found that t_r is longer and the elevation of the droplet or thick film decreases with Bi just as that found for the negative gravity cases. In contrast to the cases of $\mathscr{M} = -5$, there is no qualitative change in topological structure with $\mathscr{M} = -1$ (e.g., ridges and trapped droplet are suppressed with Bi in the former). Recalling Fig. 7, in both cases of $G < 0$ and $G > 0$, an increase in Bi suppresses the droplets and capillary ridges and it is thus inferred that the ambient cooling plays a stabilizing role, as indicated intuitively by t_r. From a mechanical point of view, weaker surface deflection acts to reduce the local curvature and thus the Laplace pressure; this stabilization is associated with the dynamic effect of smoothing corrugations by ambient cooling that produces a lower normal-stress "jump" to resist the tendency of rupture. This is an explanation for the underestimate of $H_{\min}$ in Ref. [19], where a significant surface heat loss due to thermal convection of Bi = 0.11 was neglected. Furthermore, the influence of gravity on the flow causes an insufficient representation of the DC for the numerical result, as shown in Fig. 10(c) and discussed later in Sec. VI B.

Figure 11 shows the flow-field evolution of a sessile layer, which is significantly different from that shown in Fig. 12(a) of Ref. [8], uncovering the peculiarity of the present mechanisms. The convective cells, again twice the localized trough(s) in number, are demarcated by the dividing streamlines. The convection is not recirculated because there is no closed streamline, differing obviously from the $G < 0$ case. However, their thermal fields are similar and both tend to be more distorted near the lateral sides of the valley. Under the destabilizations of vapor recoil, thermocapillarity, and buoyancy, the fluid is transported from the depressions to the bulges, which results in the amplification of deformation. The formation of a drained region preceded by convective cells was also observed by Orell and Bankoff in (0.86–1.321)-mm evaporating ethanol layers [68]. In Fig. 11(a), a shallow valley forms and liquid flows away from the depression near the interface. As the valley deepens and viscous resistance increases, against which the capillary-pressure gradients must drive fluid outward, capillary ridges emerge from the bottom and either side of the valley [Fig. 11(b)]. While liquid is pushed from the drained region to the ridges and thick-film regions, the latter collect fluid from the adjacent localized depressions as well. The flows cause the growth of the capillary ridges and the spreading of the drained region. The convection is prevailing in the upper region, while in the lower part velocity is relatively low (even stagnant), as observed in cooled evaporating layers [9]. In addition, as presented in the insets, the local flow patterns in the middle ridges are similar to the convection in the early stage shown in Fig. 11(a) but with a higher velocity, which again implies a self-affinity (Sec. VI B).

With the formation of capillary ridges on the sides of valley, the original large convective cell in the thick-film region is divided into three small ones in Fig. 11(c). The transition could support the coexistence of LW and SW modes, analogous to but different from that observed by VanHook *et al.* [7,8]. Similar mode interaction in the presence of interfacial mass transfer has been studied
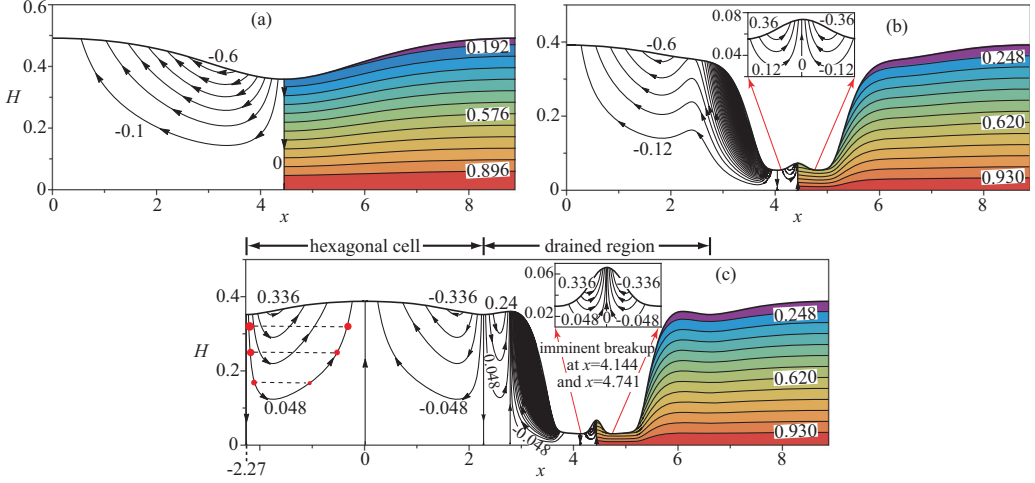
FIG. 11. Streamlines and isotherms of the case I evaporating layer for $G > 0$ at three representative moments, calculated for $\lambda = 2\sqrt{2}\pi$, $K = 0.1$, $\mathscr{E} = 0.05$, $\mathscr{D} = -1$, $\mathscr{M} = -5$, $\mathscr{G} = -0.2$, and Bi $= 1$ with a mesh of 201 points. Contours are separated by intervals of $\Delta\Psi$ and $\Delta\Theta$. (a) Initial stage of valley formation ($\Delta\Psi = 0.1$ and $\Delta\Theta = 0.064$) at $t = 10$. (b) Emergence of capillary ridges ($\Delta\Psi = 0.12$ and $\Delta\Theta = 0.062$) at $t = 11.35$. (c) Formation of the drained region just before rupture ($\Delta\Psi = 0.096$ and $\Delta\Theta = 0.062$) at $t = 11.42$. At the same level liquid is warmer under a convex surface than that under a concave one. The smaller dot denotes lighter fluid particle, illustrating the destabilizing effect of buoyancy. The hexagon wavelength [24] $\lambda_6 = \frac{3}{2}l_6 \approx 3.9$ with the side length $l_6 = \frac{2}{\sqrt{3}} \times 2.27 \approx 2.62$. The insets show the enlarged middle ridges.

theoretically for solutocapillary instability [20]. Taking a planform, a hexagon can be constituted by two families of half-torus streamlines of two contiguous periods at, say, $x = 0$, in which fluid flows downward along the cell peripheries ($x \approx \pm 2.27$) to the interior where it is heated while traveling inward and then upward around the center ($x = 0$) with the help of the buoyancy effect. In particular, the warm upflow under a convex surface consists of the characteristics of local buoyancy-driven convection in accordance with the analysis by Jeffreys [69] and the qualitative criterion of Scriven and Sternling (see [17], Sec. 7). We emphasize that the interfacial deformation originates from the Marangoni rather than the buoyancy effect (see also Sec. VI A) within the Boussinesq approximation. Nonetheless, it turns out that the LW deformation is in favor of the buoyancy convection when considering the slight expansion of buoyant liquid in the gravitational field, as shown in Fig. 11(c) for a cell. To balance the pressure due to a heavier fluid column in the periphery, the lighter central particle can be elevated relative to the cooler one on the same level (cf. left panel of Fig. 13).

The relative importance of buoyancy and thermocapillarity could be quantified by $\mathrm{Bo}_d = \frac{\mathscr{G}}{\mathscr{M}_{\mathrm{eff}}} \approx 0.05$. [Remember that Marangoni flow is mitigated by ambient cooling and volatility as $|\mathscr{M}| < |\mathscr{M}_{c,\mathrm{Bi}=0.5}^+| < |\mathscr{M}_{c,\mathrm{Bi}=1}^+|$ (see Sec. V C). With a 17.5% magnification in $|\mathscr{M}_c^+|$ for Bi $= 0.5$, a conservative estimate $\mathscr{M}_{\mathrm{eff}} \approx -4.25$ from a linear extrapolation.] This suggests that the thermocapillary effect is the main driving force of the viscous flow. As for the nonevaporating thin-film experiment of VanHook *et al.* [7], we recognize that buoyancy is negligible in that case and the small-scale hexagon is due essentially to thermocapillarity [$\mathrm{Bo}_d \approx 0.01$ for Fig. 5(c) therein]. In view of the weakened Marangoni effect, we emphasize that in the thick-film region the buoyancy can play a significant (but not dominant) role although the thermocapillary and vapor recoil effects still dominate. The horizontal scale of the hexagon, one order of magnitude larger than its thickness, is similar to that of the drained region. This could support a tight coupling between buoyancy and thermocapillary effects during evolution through reinforcing energy generated by the influence of each on the other [14] [see Eq. (34b)]. Thermocapillary deformation changes locally the depth of the
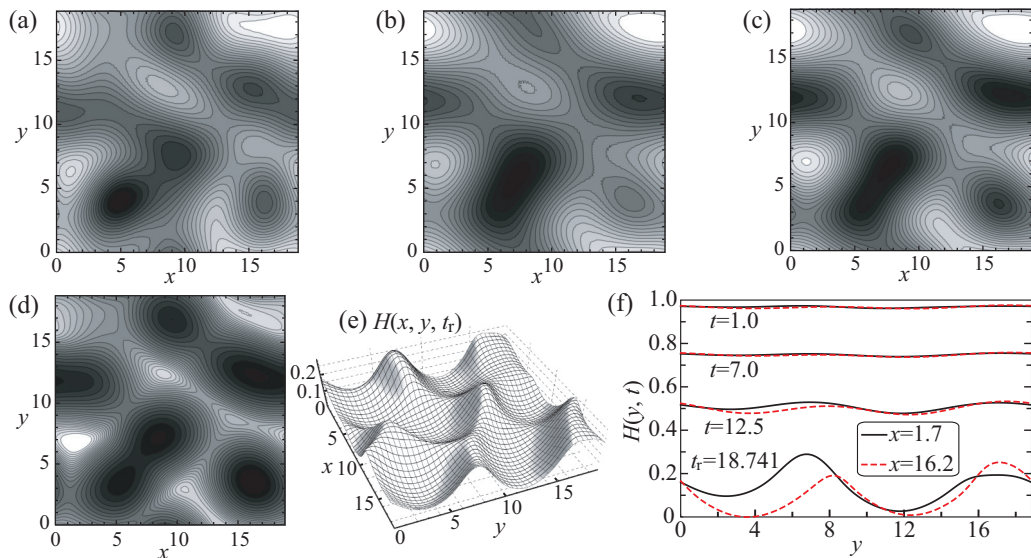
FIG. 12. Evolution of the case III evaporating layer lying on a substrate for $K = 1$, $\mathscr{E} = 0.1$, $\mathscr{D} = -0.1$, $\mathscr{M} = -5$, $\mathscr{G} = -0.1$, and Bi $= 1$ with a 171×171 mesh. The side length of the periodic domain is 6π. The amount of coupled ODEs to be solved at each step is 28 900. Successive snapshots of the interface contour with the minimum and maximum elevations ($H_{\min}$ and $H_{\max}$) are shown at (a) $t = 1$ (0.9559 and 0.9766), (b) $t = 7$ (0.7330 and 0.7586), (c) $t = 12.5$ (0.4688 and 0.5350), and (d) $t_r = 18.741$ (5.5066×10^{-5} and 0.2526). (e) Surface plot at t_r. (f) Evolution of representative profiles for $x = 1.7$ and 16.2.

layer and leads to a space-dependent temperature difference, which modifies Ra locally and hence the intensity of Rayleigh convection. The additional long-scale convection, in turn, generates mean heat and mass fluxes connected with the deformation. The convection pattern in Fig. 11(c) here is reminiscent of Fig. 1 of Ref. [70] for a nonevaporating layer subject to buoyancy and thermocapillarity with an undeformable surface. It is important to note that the deformation plays a crucial role in the long-scale convection, which makes it different from the classical hexagon [6,70]. Therefore, the evaporative convection, subject to coupled effects of surface-tension stresses and buoyancy, is preferably regarded as LW Marangoni-Rayleigh-Bénard convection, where the order of those two influences suggests their relative importance.

The streamlines are concentrated at the lateral sides of the valley in Figs. 11(b) and 11(c), where the local velocity is larger. This region can be confined by a dividing streamline [Fig. 11(c)] that does not perturb the outer domain significantly, consistent with Ref. [8]. With the expansion of the drained region, the convective cells are squeezed and the local velocities increase further, causing the well-defined capillary ridges. The drained region expels about $\frac{1}{4}$ fluid of the interval, which compensates for mass loss from the thick-film region. In contrast to the quasiequilibrium case [32], $\Delta\Theta$ across the layer is not constant along the interface (see Figs. 8 and 11). Actually, the temperature gradient at the trough is less than that of the quasiequilibrium case with the identical evaporation parameters $\mathscr{E}$ and $\mathscr{D}$; the local evaporation rate and thus vapor thrust are expected to be smaller under nonequilibrium. Hence, the smoothing effect of capillarity is adequate to balance the reduced vapor recoil, which acts as the first reason for the absence of a sharp dryout point (the other given in Sec. VI A).

Equation (25) is then solved on a square domain of $l = 6\pi$ with the IC (27b) for $G > 0$. A typical case III rupture process is exhibited in Fig. 12 for the identical parameters in Fig. 9 but with a reversal of the sign of $\mathscr{D}$ and $\mathscr{M}$. Again, there are three stages (see movie 2 in the Supplemental Material [66]): (i) The first stage is similar to that of the $G < 0$ case; (ii) depressions slowly broaden, deepen,
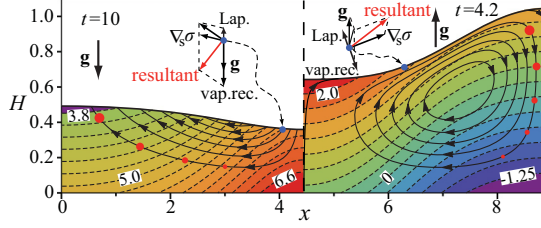
FIG. 13. Streamlines and pressure contours of case I at the emergence of a valley, calculated for $\lambda = 2\sqrt{2}\pi$, $K = 0.1$, $\mathscr{E} = 0.05$, $|\mathscr{D}| = 1$, $|\mathscr{M}| = 5$, $\mathscr{G} = -0.2$, and Bi = 1 with a mesh of 201 points. The $\hat{P}$ contours are dashed with an interval of $\Delta\hat{P}$. The parameters on the left are $G > 0$, $\Delta\Psi = 0.1$, and $\Delta\hat{P} = 0.2$; on the right $G < 0$, $\Delta\Psi = 0.016$, and $\Delta\hat{P} = 0.25$. A smaller dot along a streamline denotes a lighter fluid particle due to buoyancy. The distinct differences when streamlines cross the interfaces can be understood from a mechanical point of view, as in the insets, which are qualitative sketches illustrating the composition of forces on the interfacial particles.

and coalesce, driven by instability of the evaporating interface; and (iii) depressions develop at a faster rate to expel liquid leading to an irregularly polygonal network of ridges separated by drained regions. As a consequence of the stabilizing gravity and surface tension the dynamics results in approximately uniform thinning in space and time before $t \approx 12$, where the difference in elevation is about 0.03. In accordance with Fig. 12(f), the level descending contributes to the surface waves by reducing the stabilizing role of gravity, as observed by Kavehpour *et al.* [71] in the volatile liquid films. The relatively low ridges ($H \approx 0.25$) at rupture are in contrast to the negative gravity case in Fig. 9(d), where the typical height is larger by one order of magnitude. This is ascribed primarily to the ridges feeding liquid into surrounding valleys where more evaporation occurs and secondarily to mass loss from the ridges themselves over the longer duration under positive gravity.

The rupture pattern in Figs. 12(d) and 12(e) possesses the well-defined lateral length and height scales. This is in sharp contrast to the comparable case without evaporation where coarsening to a larger droplet is observed at rupture, as illustrated in Fig. 2(b), in which Bo $= 3.33 \times 10^{-3}$, $\mathscr{M} = -7.5$, the rescaled side length $l = 4\pi\sqrt{\text{Bo}}/k_m \approx 10.72$, and the height scale is about 2.5. The comparison suggests that evaporation could be used for controlling and creating a pattern with prescribed length scales. The LW surface pattern featuring irregular depressions with wavy rims is similar to the experimental results of VanHook *et al.* [8] [their Figs. 22(b) and 22(c)], where the film possessed proper initial thickness and the Marangoni number is well above a critical value. However, the surrounding thick-film region observed in the experiment [8] is absent in our results. It is not surprising since there is no chance to develop a large drained region surrounded by thick films under moderate mass loss, as in Fig. 17(c) as well, which never occurred in their experiment. In addition, the overall patterns depicted in Figs. 12(b) and 12(c) are qualitatively analogous to that observed by Berg *et al.* [11] in the evaporating layers [see their Fig. 7(c) for 3 mm of benzene and Figs. 10(a) and 10(e) for 1 mm of acetone and *n*-heptane for the similarity]. The typical length scales in their Fig. 10(a) and our Fig. 12(c) are one order of magnitude larger than the respective thickness. Their analyses also corroborate the simultaneous introduction of thermocapillary and buoyancy effects.

C. Effects of gravity and ambient cooling and critical $\mathscr{M}$ ($G > 0$ and $G < 0$)

With Eqs. (B3) and (23) and the transformation (15), the rescaled pressure is found to be

$$\hat{P}(x,z,t) \equiv P_0/(k|B|) = -3H_{xx} \pm \tfrac{3}{2}\mathscr{D}J_0^2 \pm (H - z)\left\{\mathscr{G}\left[\tfrac{1}{2}(H + z)f - 1\right] - 3\right\}. \qquad (38)$$

In Fig. 13 the pressure profile together with streamlines at the early stage is plotted for Fig. 8(a) at $t = 4.2$ and Fig. 11(a) at $t = 10$. The direction of gravity combined with buoyancy is found to serve as an important control on the interface stability and the flow field.
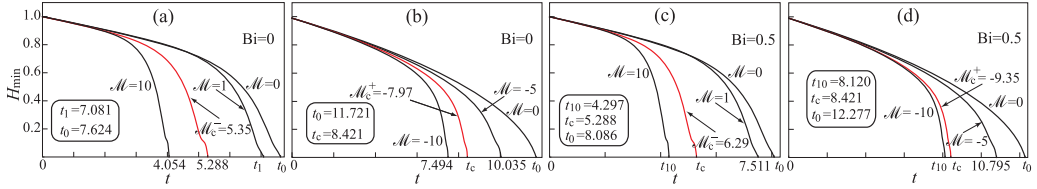
FIG. 14. The $H_{\min}$ evolution of the case I evaporating layers with different thermocapillarity for $\lambda = 2\sqrt{2}\pi$, $K = 0.1$, $\mathscr{E} = 0.05$, $|\mathscr{D}| = 1$, $\mathscr{G} = 0$, Bi $= 0$ or 0.5, and (a) and (c) $G < 0$ and (b) and (d) $G > 0$.

Interfacial fluid elements are subject to gravity, vapor recoil, Laplace pressure, and Marangoni stresses against viscous forces (see the insets in Fig. 13 for those near the troughs). For $G > 0$, they flow towards the warmer interior under the resultant force and then return to the interface under a favorable pressure gradient $\nabla \hat{P}$. It is reflected by the roughly hyperbolic pattern, contributing to the understanding of the symmetric convection cells caused by buoyancy and thermocapillary mechanisms in evaporating layers, as explained in Ref. [68]. For $G < 0$, the resultant force acting on the fluid particles just inside the free surface results in the top layer swept aside with the help of thermocapillarity while cooled by ambience and evaporation. The intersection of the streamline $\Psi = 0$ and interface is an indication of mass loss. A larger interfacial pressure at the trough is due to the opposite direction of vapor recoil and gravity. Then fluid is pushed towards the low-pressure interior along the cell partition ($x = 2\sqrt{2}\pi$) by a sufficient $\nabla \hat{P}$ arising from hydrostatic and Laplace pressures, although the buoyancy resulting from surface cooling retards this flow. The recirculation is developed by continuity, suggesting that the Marangoni effect has reached an extent sufficient to dominate the flow regime according to the criterion in Ref. [17]. Therefore, this evaporation-driven flow for $G < 0$ can be attributed with confidence to thermocapillarity and considered as LW Marangoni convection as buoyancy exerts a stabilizing influence for this flow.

Figure 14 exhibits the influences of G, Bi, and $\mathscr{M}$ on evaporation of case I with $\mathscr{G} = 0$. With different $\mathscr{M}$, it is found that t_r could be greater or less than the relevant quasiequilibrium result, thus a critical value $\mathscr{M}_c^{\pm}$ can be found in the nonlinear regime, where the superscript $+ (-)$ denotes positive (negative) gravity. In Figs. 14(a) and 14(b) for Bi $= 0$, with $\mathscr{M}_c^- = 5.35$ and $\mathscr{M}_c^+ = -7.97$ the $t_r = 5.288$ and 8.421 coincide with the corresponding quasiequilibrium results in Fig. 5(a) and Fig. 9(a) of Ref. [32]. Accordingly, one interesting remark about the dual role of volatility (proportional to K^{-1}) can be drawn. With $|\mathscr{M}| > |\mathscr{M}_c^{\pm}|$, the nonequilibrium effect destabilizes relative to quasiequilibrium by the induced thermocapillarity that counteracts the intrinsic stabilization of K; with $|\mathscr{M}| < |\mathscr{M}_c^{\pm}|$, the intrinsic stabilizing effect overcompensates the thermocapillary destabilization and gives rise to a net stabilization. Chauvet *et al.* [12] provided relevant experimental verification and a physical explanation on the opposite effects associated with volatility. Furthermore, the linear theory described by Eq. (34a) predicts the quasisteady value $\mathscr{M}_{c,s}^{\pm} = \mp 3$ for a small K. The discrepancies from the nonlinear results are due to mass loss being present here (though to a weak degree) and the interface being far enough from equilibrium ($K = 0.1$) in the full nonlinear unsteady simulation.

Figures 14(a) and 14(c) show that $\mathscr{M}_c^- = 6.29$ for Bi $= 0.5$ is larger than $\mathscr{M}_c^- = 5.35$ for Bi $= 0$ by 17.6%; with Bi $= 0.5$, the t_r for $\mathscr{M} = 1$ and 10 are both greater than those obtained with Bi $= 0$ by about 6.0%. Similarly, in Figs. 14(b) and 14(d), $|\mathscr{M}_c^+| = 9.35$ for Bi $= 0.5$ is higher than $|\mathscr{M}_c^+| = 7.97$ for Bi $= 0$ by 17.3%, in good agreement with $G < 0$; for Bi $= 0.5$, the t_r for $\mathscr{M} = -10$ and -5 are longer than those for Bi $= 0$ by 8.4% and 7.6%, respectively. The larger $|\mathscr{M}_c|$ and longer t_r (for the same $\mathscr{M}$) in both cases reflect the fact that thermocapillarity is less effective for Bi > 0 because ambient cooling weakens the temperature variation along the interface, a stabilization that the thermocapillary effect has to overcome to rupture the layers. This point has also been indicated by Burelbach *et al.* [19] in the experiments with an actually evaporating silicone-oil layer (e.g., $h_0 = 1.684$ mm, $k \approx 0.6$, and Bi $= 0.11$). Therefore, Eq. (25) should be more applicable in predicting the pattern formation of finite-thickness evaporating layers for which the cooling effect
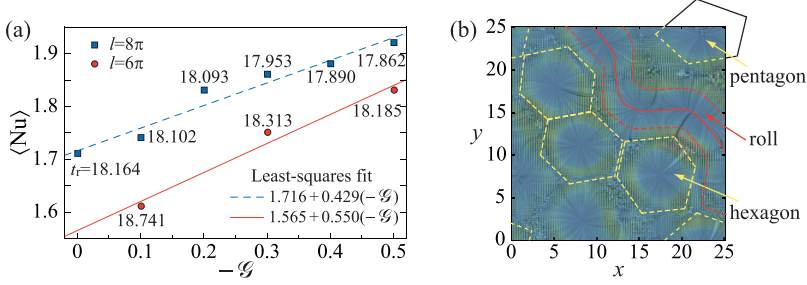
FIG. 15. Influences of buoyancy on the case III evaporating layers lying on a substrate with $K = 1$, $\mathscr{E} = 0.1$, $\mathscr{D} = -0.1$, $\mathscr{M} = -5$, and Bi $= 1$. (a) Variation of $\langle \text{Nu} \rangle$ at t_r with $\mathscr{G}$. Squares are for $l = 8\pi$ with a 181×181 mesh, circles are for $l = 6\pi$ with a 171×171 mesh, and the markers are labeled with values of t_r. (b) Line integral convolution plot for the case with $\mathscr{G} = -0.2$ and $l = 8\pi$ at t_r.

of the surroundings can play a stabilizing role. Furthermore, with $|\mathscr{M}| = 10$, the 8.4% extension in t_r for $G > 0$ is larger than 6.0% for $G < 0$ due to the stabilization of gravity. The comparisons of t_r for $|\mathscr{M}| = 0$ and 10 in each pair of cases with Bi $= 0$ or 0.5 reveal the stabilizing role of gravity as well.

D. Effect of buoyancy on the evaporating layer with positive gravity

Before proceeding to the influence of buoyancy on profile evolution, we note that, for the case of $G > 0$, Kimball *et al.* [43] showed that the buoyancy mechanism contributes to the instability of evaporative convection and increases the liquid heat-transfer coefficient $h_{\text{th}}^{(l)}$. Thus, it is worth considering its influence on heat transfer in a sessile evaporating layer. The heat flux at the solid-liquid interface $q_w = -k_{\text{th}} \theta_z|_{z=0} = h_{\text{th}}^{(l)}(\theta_w - \theta_I)$, whence $h_{\text{th}}^{(l)}$ can be evaluated as

$$h_{\text{th}}^{(l)} = \frac{-k_{\text{th}} \theta_z|_{z=0}}{\theta_w - \theta_I} = \frac{-k_{\text{th}} \Theta_z|_{z=0}}{\Theta_w - \Theta_I}, \tag{39}$$

where $\Theta_w = 1$ and $z = Z$. Choosing the average thickness h_{av} as the characteristic length, the local Nusselt number is given by

$$\text{Nu} = \frac{h_{\text{th}}^{(l)} h_{\text{av}}}{k_{\text{th}}} = \frac{-\Theta_z|_{z=0} \langle H \rangle}{\Theta_w - \Theta_I}, \tag{40}$$

where $\langle \cdot \rangle = l^{-2} \int_0^l \int_0^l dx\, dy (\cdot)$ is defined as the average over the square domain. We then numerically evaluate the average Nusselt number of the layer by

$$\langle \text{Nu} \rangle = \frac{\langle H \rangle}{l^2} \int_0^l \int_0^l \frac{dx\, dy}{H} = \langle H \rangle \langle H^{-1} \rangle. \tag{41}$$

As shown in Fig. 15(a), as the contribution of buoyancy increases, $\langle \text{Nu} \rangle$ tends to increase. The trend suggests an increasing importance of convective heat transfer, which appears to be more significant for a shorter l. The ridges become more obvious as warm fluids rise over the wide interior of the polygons or rolls and collect along the cell partitions, where cooled surface liquid becomes unstable and flows down to form evaporation convection. Meanwhile, t_r is slightly shortened with an increase in $|\mathscr{G}|$. These reflect that the convection and heat transfer characteristics have been changed when buoyancy takes effect in the unstable layer. Thus the buoyancy effect indeed contributes to destabilizing the surface, although its influence on t_r and deformation is much less than that of the Marangoni effect within the Boussinesq approximation.

A representative example of the numerical flow is visualized in Fig. 15(b) by means of line integral convolution [72]. The technique can generate a vector-field representation for the computed
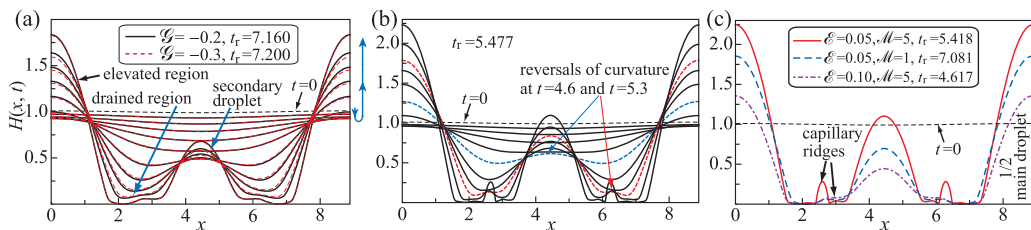
FIG. 16. Results for $G < 0$, $K = 0.1$, and $\mathscr{D} = 1$ with a mesh of 201 points. Case I evolution with $\mathscr{E} = 0.05$ is shown for (a) $\mathscr{M} = 1$ and $\mathscr{G} = -0.2$ or -0.3 at $t = 1,2,3,4,5,6,6.5,6.8,7,t_r$ and (b) $\mathscr{M} = 5$ and $\mathscr{G} = -0.2$ at $t = 1,2,3,4,4.6,5,5.2,5.3,5.4,t_r$. (c) Rupture patterns of cases I and II with $\mathscr{G} = 0$.

horizontal velocity of the interface from Eq. (26), convolved with an initially rasterized image of a random pixel, to simulate the fluid motion with tracer particles by tracing streamlines with a certain arc length over the entire surface. The convective pattern is a combination of irregular LW hexagons, sinuous rolls, and polygons over the expanding valleys, which could be linked to the Marangoni, buoyancy, and evaporation effects [4,9]. It is shown that the primary pattern is hexagonal-like since the convection in the evaporating layer is dominated by the thermocapillary effect. The local smearing near cell peripheries may be due to the insufficient vector length at the relatively narrow ridges. Nevertheless, this analysis has a limitation of fixed parameters that prevents us from capturing a possible transition between the patterns [4]. For example, supercriticality would decrease with t if Ma had been calculated with instantaneous values of $\Delta\theta(t)$ and $h(t)$.

The flow patterns in Fig. 15(b), especially the vermiculated rolls, resemble closely that observed by Zhang [9] in the evaporating R-113 layers with $h_0 = 1$ mm and $\theta_w > \theta_I$, as can be seen in Zhang's Figs. 8(a)–8(c) and 10(c), where the flow was visualized by seeding with aluminum powders. The wavelength of the hexagonal-like convection [24], $\lambda_6 = 3l_6/2 \approx 6.7$, with l_6 being the average side length, is larger than the experimental result of $\lambda_6 \approx 6$ for the Bénard-type cells in 0.2- (0.32-) mm evaporating R-113 layers (corresponding to case III without buoyancy) heated (cooled) below [9]. This should be a buoyancy-driven response mode. It is therefore reasonable to infer that the coexistence of polygons and rolls, the flow analysis for Fig. 11, and the larger λ_6 with buoyancy effect together give an indication of the LW Marangoni-Rayleigh-Bénard convection in the evaporating layers with positive gravity.

VI. PROFILE EVOLUTION

We have considered time-dependent simulations with emphasis on ambient cooling, flow field, and $(2 + 1)$D pattern formation. The subject of Sec. VI A is to understand the interfacial behavior influenced by mass loss and buoyancy up to the first rupture. The resulting patterns motivate us to investigate a hierarchical structure via *successive* ruptures in Sec. VI B stressing the interfacial fractal in the absence of gravity and mass loss, as speculated recently in Ref. [51] in passing. Both sets of studies include the essential evaporation effects of thermocapillary convection and vapor recoil. Comparisons of the drop profiles in Secs. V and VI A with DCs in Sec. VI B suggest an imperfect fractal due to mass loss and gravity.

A. Influences of buoyancy, thermocapillarity, and mass loss ($G > 0$ and $G < 0$)

We now focus on the effects of gravity combined with buoyancy, thermocapillarity, and mass loss on the profile evolution that are seen more clearly in the $(1 + 1)$D simulation on a small domain [50] of $\lambda = 2\sqrt{2}\pi$ without ambient cooling (Bi $\to 0$), where thermal energy transferred to the interface through the liquid is converted entirely to latent heat. Equation (25) is solved in the $(1 + 1)$D version with the IC (27a) for different $\mathscr{G}$ and $\mathscr{M}$ in cases I and II.
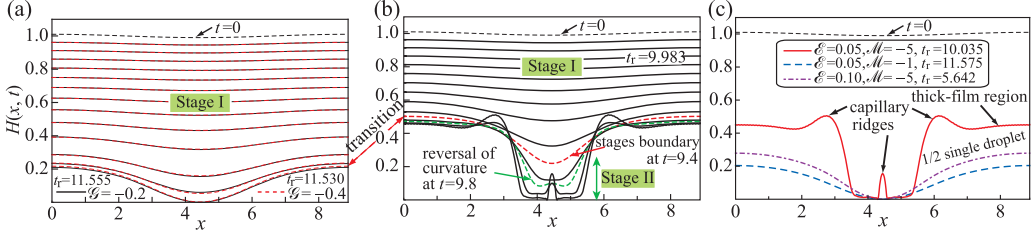
FIG. 17. Results for $G > 0$, $K = 0.1$, and $\mathscr{D} = -1$ with a mesh of 201 points. Case I evolution with $\mathscr{E} = 0.05$ is shown for (a) $\mathscr{M} = -1$ and $\mathscr{G} = -0.2$ or -0.4, corresponding to $0 \leqslant t \leqslant 11$ with $\Delta t = 1$ and instants of 11.4 and t_r, and (b) $\mathscr{M} = -5$ and $\mathscr{G} = -0.2$ at $t = 1,2,3,4,5,6,7,8,9,9.4,9.7,9.8,9.92,t_r$. (c) Rupture patterns of cases I and II with $\mathscr{G} = 0$.

As shown in Figs. 16(a) and 16(b) for the case I evolution at $G < 0$, (i) the layer thins nearly uniformly during the initial $t_r/3$ as a result of mass loss and surface tension and (ii) the crest of the elevated region first slightly sinks along with the flattening of the trough under Laplace pressure and then grows quickly due to RTI [see the arrows aside Fig. 16(a)]. The rapid growth of new valleys is attributed to the intensified local vapor thrust and thermocapillarity. The weak stabilizing effect of buoyancy is revealed by Fig. 16(a), in which t_r increases merely about 0.6% with a 50% increase in $\mathscr{G}$ and the evolutions are almost identical, or by comparing the relevant results in Figs. 16(a)–16(c). For example, with $\mathscr{E} = 0.05$ and $\mathscr{M} = 1$, $t_r = 7.200$ for $\mathscr{G} = -0.3$, which is longer than the $t_r = 7.081$ for $\mathscr{G} = 0$ by only 1.7%, and the rupture patterns are essentially the same. With an increase in $\mathscr{M}$, the evolution becomes more complex and t_r is shorter, manifesting the destabilizing impact of thermocapillarity, as can be seen in Fig. 16(b): (i) Small capillary ridges are generated and droplets become higher, (ii) spreading of drained regions becomes more evident as the vapor recoil and thermocapillarity are sufficient to enlarge the deformation, and (iii) with liquid pulled from the depressions, the secondary drop and capillary ridge divide the previous valleys into two smaller ones. The transition begins with the reversal of curvature sign at the troughs, where Marangoni stresses together with vapor recoil prevail over the stabilization of capillary forces.

The differences between destabilizing and stabilizing gravity become transparent, if Figs. 16 and 17 are compared: For $G > 0$, regardless of whether buoyancy is present or not, only one big droplet and a drained region fit the interval without an elevated region; also, t_r remarkably increases, because the hydrostatic pressure tends to fill the valley that the vapor thrust and thermocapillarity have to overcome the flattening effect. For example, with $\mathscr{E} = 0.05$, $|\mathscr{M}| = 1$, and $\mathscr{G} = 0$, $t_r = 11.575$ is longer than 7.081 for $G < 0$ by 63.5%. Regardless of buoyancy, for a small $\mathscr{M}$ the interface develops a shallow valley under positive gravity and surface tension; however, with an adequate $\mathscr{M}$ one droplet can be trapped in the drained region and capillary ridges are generated whose crests even exceed the level of the thick-film region. This reflects also that buoyancy plays a weak destabilizing role in the interface for $G > 0$. As revealed by Fig. 17(a), the two evolutions are indistinguishable except close to rupture and t_r reduces only by 0.2% with $|\mathscr{G}|$ doubled from 0.2 to 0.4; also, we see, by comparing the relevant results, e.g., with $\mathscr{E} = 0.05$ and $\mathscr{M} = -5$, that $t_r = 9.983$ with $\mathscr{G} = -0.2$, which is earlier than 10.035 with $\mathscr{G} = 0$ by merely 0.5%, and the rupture patterns are nearly the same.

Figures 17(a) and 17(b) represent two typical evolutions. The first one is related to a small $\mathscr{M}$, in which the layer thins almost uniformly during the early stage. The evolution is then accelerated especially at the wavelength midpoint because the local vapor recoil and thermocapillary instabilities dominate over the capillarity and gravity, according to our linear theory [see Fig. 6(d)]. The valley eventually touches the substrate with zero contact angle in contrast to the sharp troughs in quasiequilibrium [32]. The profiles of the drained region are similar to that observed by Orell and Bankoff [68] with evaporating ethanol of $h_0 = 1.092$ mm (see their Fig. 2). The second one is associated with large $\mathscr{M}$, divided into two stages with the boundary occurring at $t = 9.4$. The first

stage is similar to the small-$\mathcal{M}$ case or a quasiequilibrium early evolution in Fig. 9(a) of Ref. [32], suggesting that the initial stabilizations of gravity and capillarity are adequate but overcome by vapor recoil and thermocapillarity later. The second stage starts with the flattening of the trough whose curvature then reverses until rupture. From Fig. 17(b) one can identify (i) a shorter t_r, (ii) the emergence of well-defined capillary ridges, (iii) the broadening of the drained region that covers the substrate with a thinning film, analogous to those found by VanHook *et al.* [7] using 0.05–0.25 mm of silicone oil subject to a supercritical temperature difference [see their Figs. 3 and 5(c)], and (iv) the thinning of the thick-film region being damped, as discussed in Sec. V B, to form a flattened droplet.

As for the well-defined capillary ridges emerging with large $\mathcal{M}$, explained by the flow field in Sec. V B, there are two additional reasons related to the small $\mathcal{E}$ ($\propto E\,\Sigma_0$) of case I: (i) the fluid, squeezed quickly to the rim of the thick-film region, overcompensates for the amount of local evaporation (low E) and (ii) the replenishing flow causes a fast increase in local normal stresses capable of deforming the adjacent interface under weak capillary pressure (small Σ_0). Furthermore, for both cases at $G < 0$ and $G > 0$, there is no chance to develop the ridges in case II even with a strong Marangoni effect, shown as dot-dashed lines in Fig. 16(c) and Fig. 17(c), caused by the sufficient surface tension and evaporation rate under a moderate $\mathcal{E}$. Therefore, an increase in $\mathcal{E}$ suppresses the capillary ridges and droplets.

We now turn to the two reasons for the large-scale drained region. The first one, related to the reduced vapor recoil, was explained in Sec. V B. The other is associated with the thermocapillarity resulting from nonequilibrium. The viscous resistance within the depression becomes larger as it thins down, while σ increases away from the trough along the lateral sides of valley. At an increasing distance from the trough during evolution, the two forces can reach a dynamical balance, enabling pressure to uniformize underneath the drained region and vapor recoil to push the rounded valley in a distributed mode, thus the trough tends to expand. On the contrary, in quasiequilibrium [32] there is no Marangoni stress to draw the fluid away from a valley that allows the *localized* vapor thrust to cause the sharp rupture with the localized trough(s). To summarize, the evolution of the evaporating layer is sensitive to the direction of gravity and depends strongly on $\mathcal{E}$ and $\mathcal{M}$ but not $\mathcal{G}$.

B. Dissipative compactons and interfacial fractal

To relate the droplets with zero contact angle in a final profile to DCs, the buoyancy term can safely be disregarded as compared to the thermocapillary effect. For case I, mass loss is less important and is neglected for the moment. To alternatively support the conclusions about the gravity effect, we further eliminate the gravity term. In the $(1 + 1)$D case, Eq. (25) thus reduces to

$$H_t + (H^3 H_{xxx})_x + [H^2 f J_0(K|\mathcal{M}|) + |\mathcal{D}|H J_0)H_x]_x = 0, \tag{42}$$

where the different algebraic signs in $\mathcal{M}$ and $\mathcal{D}$ have been unified [cf. Fig. 1(b)]. To seek the touchdown steady-state symmetric localized solution [73] $H = \mathcal{H}(x) \geqslant 0$ of Eq. (42), after the first integral we arrive at [the constant of integration must vanish (see [73], Theorem 2.1)]

$$\mathcal{H}\mathcal{H}''' + f(\mathcal{H})J_0(\mathcal{H})[K|\mathcal{M}| + |\mathcal{D}|\mathcal{H} J_0(\mathcal{H})]\mathcal{H}' = 0, \tag{43}$$

where the prime denotes d/dx. The nonlinear ODE has a steady compact support solution with maximum $\mathcal{H}_m = \mathcal{H}(x_m)$, nonvanishing on its support $|x - x_m| \leqslant l_n < \infty$ $(n \in \mathbb{Z}^+)$,

$$x + c_2 = \pm \frac{1}{\sqrt{2}} \int_1^{\mathcal{H}(x)} \left\{ c_1\chi - \frac{|\mathcal{D}|J_0(\chi)}{2(1 + \mathrm{Bi}K)} - (1 + \mathrm{Bi}K)\frac{|\mathcal{M}|}{K}\chi \ln[\chi J_0(\chi)] \right\}^{-1/2} d\chi, \tag{44}$$

where $c_1 = \frac{|\mathcal{D}|J_0(\mathcal{H}_m)}{2(1+\mathrm{Bi}K)\mathcal{H}_m} + (1 + \mathrm{Bi}K)\frac{|\mathcal{M}|}{K}\ln[\mathcal{H}_m J_0(\mathcal{H}_m)]$ and $c_2 = -x_m \pm \frac{1}{\sqrt{2}}\int_1^{\mathcal{H}_m}(\cdot)d\chi$, with $(\cdot)$ being the integrand in Eq. (44) for $\mathcal{H}_m > 1$ and $c_2 = -x_m$ for $\mathcal{H}_m \leqslant 1$.

Here we demonstrate that the inverse-function solution in Eq. (44) represents a self-affine set (see [74], p. 350) parametrized by $\mathcal{H}_m$ via comparing the numerical result of the time-dependent
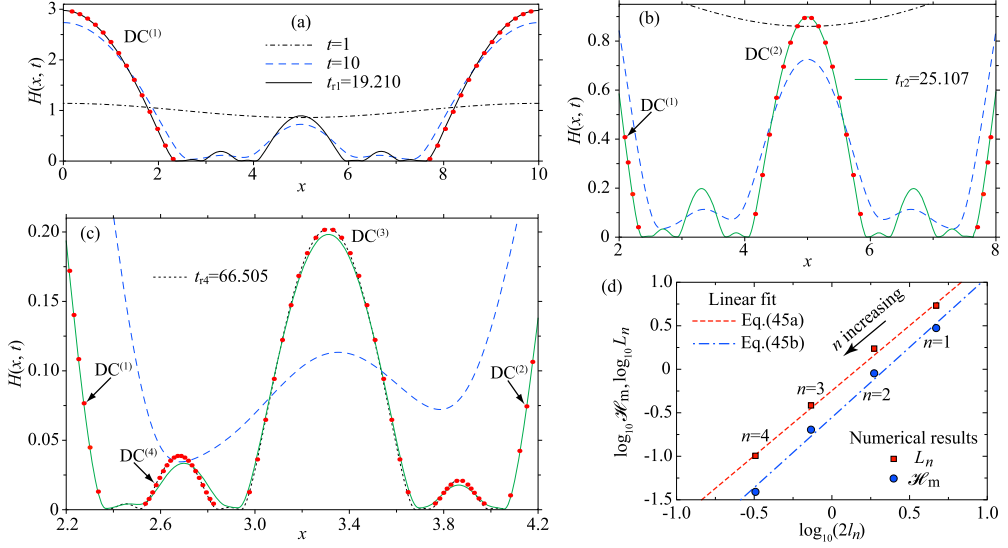
FIG. 18. Hierarchical DCs indicate the self-affine structure of Eq. (44). (a)–(c) Evolution of $H(x,t)$ illustrates droplet formation for $K = 1$, $|\mathcal{M}| = 5$, $|\mathcal{D}| = 0.1$, and Bi $= 0.1$ using the IC (27a) with $\varepsilon_0 = 0.1$. Lines represent numerical results of Eq. (42) and circles show the corresponding DCs with Eq. (44). (b) and (c) show close-ups of the imminent DCs in (a). (d) Plot of L_n and $\mathcal{H}_m$ versus $2l_n$.

simulation of Eq. (42) having local maxima $H_m^{(n)}$ to a hierarchical structure of DCs family with $\mathcal{H}_m = H_m^{(n)}$, as shown in Figs. 18(a)–18(c). Equation (42) is discretized in $[0,10]$ with 10^3 nodes and solved with the numerical method presented in Sec. III B. To efficiently resolve the structure on smaller scales as in Ref. [49], we iteratively delete the interval(s) occupied by the DC$^{(n)}$ formed from the computational domain after rupture at t_{rn} and then impose the BCs and deploy the available resolution for the still evolving intervening domain(s) via Eq. (44) until the next rupture at $t_{r(n+1)}$, which enables us to capture up to DC$^{(4)}$. By this means we examine the transition as the period decreases, which is distinct from the numerical continuation technique employed in Ref. [50] to study the property of compact support solution as a function of period. The set of surviving intervals constructs a Cantor-set-like fractal. The fractalization process can be described as consecutively replacing the troughs between DCs by increasingly smaller stationary DCs into a hierarchical structure. Theoretically, this process is continued *ad infinitum*.

To quantify the fractal properties, the functional relation between the distance L_n of two adjacent DCs of nth and $(n-1)$th orders and the support $2l_n$ of DC$^{(n)}$, as well as that between $\mathcal{H}_m$ and $2l_n$, are illustrated in Fig. 18(d). The results follow the power laws

$$L_n \approx c_L(2l_n)^{m_L} \tag{45a}$$

and

$$\mathcal{H}_m \approx c_{\mathcal{H}}(2l_n)^{m_{\mathcal{H}}}, \tag{45b}$$

with $c_L \approx 0.56$, $m_L \approx \frac{3}{2}$, $c_{\mathcal{H}} \approx 0.28$, and $m_{\mathcal{H}} \approx \frac{8}{5}$. It is evident from Eq. (45b) that a self-affinity extends over several scales similar to those observed in the Marangoni instability of nonevaporating films [49,50]. As $\lim_{n\to\infty} \frac{L_n}{l_n} = 0$, multidrop branches in Fig. 4 of Ref. [50] together with their scaling based on mean thickness indicate such a kind of self-affine structure as an array of drops separated by dry spots. The fractal structure of droplets emerging from the evolutionary equation (42) agrees well with the profiles obtained from Eq. (44) that possesses the property in Eq. (45b). This reveals that Eq. (44) indeed represents self-affine solutions because self-affinity is a necessary condition for

a fractal [74]. Therefore, the DC that inherently mediates the pattern formation can be identified as a primitive element responsible for the hierarchical fractal structure. From the viewpoint of energy, the fractal pattern of Eq. (42) originates from the growth of higher harmonics and is closely related to the fact that the Lyapunov functional of Eq. (25) with $\mathscr{E} = 0$ (cf. Appendix C) has a local minimum on the DC.

In Figs. 7(c) and 10(c), we compare the numerically obtained profile having $H_m^{(n)}$, $n = 1, 2$, with the corresponding DCs. It seems to be a reasonable approximation in the RTI case. The DC$^{(2)}$ deviates from the numerical result in Fig. 7(c) since the secondary drop has not yet touched down. For $G > 0$, DC$^{(1)}$ only approximates the lateral sides of the valley in Fig. 10(c). Under the stabilization of positive gravity the duration is significantly longer (here $t_{r,G>0} \approx 2t_{r,G<0}$) and the big drop tends to flatten and the valley to be filled such that higher harmonics have a chance to rapidly develop in the later stage (see the physical explanation in Secs. V B and VI A). Another source of the difference is mass loss, neglected in Eq. (44). The mass loss, together with the resulting earlier touchdown in simulations performed at $\mathscr{E} > 0$, feeds a lower $\mathscr{H}_m$ to Eq. (44) and thus a narrower DC [$l_n \propto \mathscr{H}_m^{5/8}$; see Eq. (45b)]. The comparisons imply that the fractal is defective as a result of mass loss and gravity, in contrast to the exact one obtained from Eq. (42).

As shown in Figs. 7 and 16 for $G < 0$ and Figs. 10 and 17 for $G > 0$, results for a small $|\mathscr{M}|$ reveal that the interfaces rupture prior to the emergence of higher-order DCs; however, with an adequate $|\mathscr{M}|$ and small Bi, a symmetric IC can evolve into a cascade of DCs of different amplitudes. After the first rupture the solutions have compact supports and drops standing on thin films in Figs. 7(c) and 10(c). The partially coalesced states are not energetically favorable [26], thus there exists a tendency to higher-order DCs (Fig. 18) which are more stable. The knowledge of the self-affinity of Eq. (44) and the fractal properties in Eq. (45) suggests that rupture will occur successively at the base of local higher droplets even with mass loss. For instance, in the insets of Figs. 7(c) and 10(c) the local troughs can continue evolving and a secondary instability is expected at the local minima to bear symmetric DCs of the next generation in finite time. This can also explain the transition between Figs. 7(a) and 7(b). Finally, the instability of evaporating layers could lead to a dropwise fractal-like pattern, as expected [49] in an experiment. The domain-excluding scheme can be further applied to investigate the nonconserved system. Markedly, after the formation of lower-order DCs, they should *not* remain of constant volume but continue evaporating and receding. The interfacial evolution could be regarded as quasisteady based on its long time scale relative to touchdown and the DCs formed can serve as local initial profiles. However, the evaporation dynamics of isolated droplets clearly has to do with wettability and the contact condition (see, for example, Refs. [3,57,75]), which requires a separate analysis.

VII. DISCUSSION AND CONCLUSIONS

We generalized the long-wave evolution equation to account for gravity combined with buoyancy correction and ambient cooling in an evaporating layer. The interfacial or internal dynamics and stabilities were examined with varying degree of thermocapillarity, buoyancy, and ambient cooling under negative and positive gravity in three regimes: case I, for $\mathscr{E} = O(10^{-2})$ and $\mathscr{D} = O(1)$; case II, for $\mathscr{E} = 0.1$ and $\mathscr{D} = O(1)$; and case III, for $\mathscr{E} = |\mathscr{D}| = 0.1$. The $(1 + 1)$D and $(2 + 1)$D simulations were carried out to characterize the instabilities, including t_r and surface evolution, which might reproduce the pattern formation in a quantitative way to make it possible to compare with further experiments. Special emphasis was laid on evaporative convection and interfacial fractal. The physical features of the interface and convection are in reasonable agreement with relevant experimental or numerical results. The results could be significant for enhancement of heat and mass transfer. The complexity and regularity of the patterns might be useful in the flow control technologies, where evaporation and surface deformation are essential, such as deposition patterning by transport of suspended (nano)particles in the volatile liquid films [3]. The large drained regions in evaporating layers, attributed to thermocapillarity and vapor recoil, should be avoided in cooling applications. Thus, it is important to sustain an unbroken layer of volatile liquid of large latent heat for cooling,

for example, flowing down a slightly inclined surface [50] of a high-power density. The main results are summarized as follows.

(i) There are few works in the literature on the nonlinear simulation of the coupled problem in evaporating layers and *a fortiori* on the $(2 + 1)$D problem incorporating a comparison of positive and negative gravity. Neglecting the other non-Boussinesq effects, the interface instability was found to give rise to the LW Marangoni-Rayleigh-Bénard (LW Marangoni) convection for $G > 0$ ($G < 0$), whose wavelength depends on the evaporation conditions and liquid properties (such as volatility and β). The numbers of cells in both $(1 + 1)$D cases doubled with time. For case I the $(1 + 1)$D simulations had an adequate $|\mathscr{M}|$ regardless of buoyancy: for $G < 0$ the main and secondary droplets and the large dry regions formed along with trapped capillary ridges and for $G > 0$ the capillary ridges emerged from either edge of the thick-film regions with another trapped in a single drained region. These local bulges could be suppressed with a larger $\mathscr{E}$ or Bi. In the $(2 + 1)$D simulation of case III, a random perturbation evolved into the large-scale drained regions separated by an irregular network of ridges in both cases of $G < 0$ and $G > 0$, while the height scale was one order of magnitude smaller in the latter. In the nonlinear regime, we identified the critical values of $\mathscr{M}$, demonstrated the dual role of K stated by Chauvet *et al.* [12], and showed that ambient cooling played a stabilizing role by weakening thermocapillarity and vapor recoil.

(ii) The buoyancy played a weak destabilizing (stabilizing) role in rupture instability for $G > 0$ ($G < 0$), but made contributions to the large-scale convection and heat transfer. Specifically, for case III the average Nusselt number increased with $|\mathscr{G}|$ and the hexagon wavelength with buoyancy effect was larger than that of the evaporative convection experiment [9] with negligible buoyancy. A study similar to the RTI case was performed in Ref. [28] but without buoyancy.

(iii) Even with moderate and strong vapor thrust, the rupture patterns featured the sessile or pendent drops with zero contact angle and wide troughs, in contrast to quasiequilibrium cases [31,32]. When mass loss and gravity were absent but vapor recoil was present, a dissipative compacton [49] could describe the drops. Besides a similar power law for the dry regions [49], we extracted an additional one, Eq. (45b), to characterize the complex fractal property of the droplets. It was confirmed that the DC having a nontrivial (in the sense of compactness) self-affinity acted as a *primitive element* of the hierarchical pattern. It should also appear in our nonconserved system with nonlinear dissipation. The fractalization process, however, could be defective as a result of mass loss and gravity, which imposed restrictions on experimental conditions for verification (such as ambient pressure, volatility, and liquid thickness).

(iv) The time-dependent LSA suggested that rupture instability was reinforced by the vapor recoil. The quasisteady analysis yielded a critical modified Marangoni number for small K, $\mathscr{M}_{c,s}^{\pm} = 3(\mathscr{D} - \frac{1}{20}\mathscr{G})$, relative to the quasiequilibrium case. Linear stability analysis for the general cases with Bi > 0 has been performed using the frozen-time approach to distinguish the influences and interactions of various mechanisms. For relatively small Ma, there was a critical thickness above which the interface was stable with $G > 0$. The stabilization of ambient cooling was significant only far enough from quasiequilibrium and enhanced with E. Its implications were thus assessed with $K \geqslant 0.1$ in the nonlinear simulations.

(v) We forecast a neutral locus [Eq. (34b)] for the onset of large cellular convection in a sessile layer, reminiscent of the thresholds $M_c^0 = 48$ and $R_c^0 = 320$ in the respective pure LW instabilities without evaporation [62,63]. The thresholds differed from those found by Nield [14] in the short-wave instability $M_c/M_{c,\mathrm{SW}}^0 + R_c/R_{c,\mathrm{SW}}^0 \approx 1$, where $M_{c,\mathrm{SW}}^0 = 79.6$ and $R_{c,\mathrm{SW}}^0 = 669.0$ with $k \approx 2$ at Bi $\to 0$. As in Fig. 3(b), at each value of $\mathscr{G}$, the layer was unstable above the corresponding line Ob; as $\mathscr{G}$ decreased, the stability region was enlarged from $A_2 D_2 O$ via $A_1 D_1 O$ to $A_0 D_0 Ox$. According to Eq. (34b), M_c decreases as R_c increases, thus these two instability mechanisms reinforce each other. This described a balance between the energy supplied by vapor recoil, buoyancy, and Marangoni stresses and the kinetic energy dissipated by viscosity. It also revealed the destabilizing effect of vapor recoil. That is, both critical values at the onset of respective convection instabilities were reduced by a factor of $\frac{1}{48}\mathrm{Ga}|\mathscr{D}|$ being of $O(10^{-2}$–$1)$.

(vi) We showed (in Appendix C) that with a special form of the nonconserved part, Eq. (C1) could be written as a gradient dynamics (C6) in terms of the variation of an appropriate Lyapunov functional. In other words, for some forms of evaporation term, the variational principle not only exists but also is a Lyapunov functional. Thus the computational advantage of the variational principle remained. Besides its higher computational accuracy [55] as compared to standard lubrication models, an important implication of the form was that a nonconserved dissipative system that was out of equilibrium might still follow a gradient dynamics. Such a variational structure also precluded oscillatory solutions, thus no primary or secondary bifurcations to traveling or standing waves could occur [50].

For an evaporating layer, it would be interesting also to study the interaction between the SW convection, in either the Bénard-Marangoni [20–22] or Rayleigh-Bénard mode, and the LW deformation, especially when the instability thresholds are close to each other. The onset of LW instability can further be compared with that of the corresponding SW version to decide whether the coupling of the two modes is pronounced. Such an investigation requires a system of two coupled evolution equations, one for the amplitude of the SW mode and the other for the surface deformation, to be derived with a (weakly) nonlinear analysis, which is left for future investigation.

Concerning the question of the possibility of violating the Boussinesq approximation when adding surface deformation and neglecting the other non-Boussinesq effects, one noted the following. (i) The LW theory can describe the interface evolution close to rupture [1,2,31,54]. The instability, governed by an evolution equation, always results in deformation on the order of mean thickness. Therefore, at leading order, it is reasonable to assume that the deformation can be much more significant than the other non-Boussinesq effects (e.g., variable fluid properties with temperature). (ii) The values of parameters have been chosen such that $|\mathrm{Ra}| \ll |\mathrm{Ga}|$ [23] or, equivalently, $\frac{1}{3}|\mathscr{G}| \ll 1$. With these in mind, the validity of the Boussinesq approximation can be ensured. However, when a simulation based on the assumption is compared with experiment for a liquid whose thermophysical properties are not strictly constant, deviations may arise from the non-Boussinesq contributions, which usually come from the temperature dependence of viscosity [5]. Finally, as in our case study, buoyancy along with the Boussinesq approximation can be left out by setting $\mathrm{Ra} = 0$ or $\mathscr{G} = 0$.

ACKNOWLEDGMENTS

APPENDIX A: BASIC STATE

The $O(1)$ basic state of Eqs. (10)–(14) can be obtained with the similar method in [31],

$$\bar{H}(T) = \{-K + [(1 + K + \mathrm{Bi}K)^2 - 2(1 + \mathrm{Bi}K)ET]^{1/2}\}(1 + \mathrm{Bi}K)^{-1}, \tag{A1a}$$

$$\bar{J}(T) = [(1 + K + \mathrm{Bi}K)^2 - 2(1 + \mathrm{Bi}K)ET]^{-1/2}, \tag{A1b}$$

$$\bar{\Theta}(Z,T) = 1 - (1 + \mathrm{Bi}K)\bar{J}Z, \tag{A1c}$$

$$\bar{P}_d(Z,T) = \tfrac{3}{2}E^2 D^{-1}\bar{J}^2 + G\bar{H} - \tfrac{1}{2}\mathrm{Gr}(\bar{H} - Z)[(1 + \mathrm{Bi}K)(\bar{H} - Z) + 2K]\bar{J}, \tag{A1d}$$

where the dimensionless dynamic pressure $\bar{P}_d = \bar{P} + \Phi$ is introduced for buoyancy-driven flow. Equation (A1) describes a time-dependent stationary thinning layer with a flat interface. With $G, \mathrm{Gr}, \mathrm{Bi} \to 0$, it reduces to the basic state in Ref. [31]. The physical properties of water and relevant parameters are provided in Table II for the presentation of basic-state behaviors and the further calculation. Here we set $K = 0.06$ and $\mathrm{Bi} = 10$ for illustration. As discussed in Sec. II and Ref. [57], K could be regarded as a reciprocal of interfacial Bi associated with evaporation and a greater value would be reached with a smaller a [28].

TABLE II. Physical properties [76] and evaporative parameters for water at 101.325 kPa and corresponding θ_s with $\Delta\theta = 10$ K, $a = 1$, and $h_0 = 10^{-3}$ m.

Parameter	Value
θ_s (K)	373.12
M_w (g mol^{-1})	18.02
ρ, ρ_g (kg m^{-3})	958.37, 0.5977
σ_0 (mN m^{-1})	58.917
γ (mN m^{-1} K^{-1})	0.180
ν (cm^2 s^{-1})	2.941×10^{-3}
β (K^{-1})	7.505×10^{-4}
c_p (J kg^{-1} K^{-1})	4215.6
$k_{\text{th}}, k_{\text{th},g}$ (W m^{-1} K^{-1})	0.6791, 2.509×10^{-2}
$\tilde{L}$ (kJ kg^{-1})	2256.5
D	9.35×10^{-4}
E	0.011
K	8.66×10^{-5}
Pr	1.75

For $K = 0$ with Bi $\to 0$, $\bar{H} = (1 - 2ET)^{1/2}$ vanishes at evaporation time $T_e = \frac{1}{2E}$ with velocity $\bar{H}_T|_{T=T_e} \to -\infty$; $\bar{J} = (1 - 2ET)^{-1/2}$ increases from unity to infinity as $T \to T_e$ due to the constant temperature difference across the thinning layer, $\bar{\Theta}_w - \bar{\Theta}_I = 1$ [see Figs. 19(a)–19(c)]. The singularities and nonuniformities of the solution (A1) are as follows: (i) $\bar{J} \to \infty$ as $T \to T_e$, (ii) $\bar{P}_d$ depends directly on vapor thrust, and (iii) quasisteady $\bar{\Theta}$ cannot satisfy an arbitrary IC. However, it is expected that disturbances evolve much faster than the basic-state vanishing, thus the late-time singularities do not hinder our analysis [31]. As $T \to T_e$, the inertial effect, required to be small by LW theory, is significant as higher-order terms become important, which will be resolved by the terminating criterion in our numerical method (see Sec. III B).

When $K > 0$ and finite, $\bar{H}$ vanishes at $T_e = \frac{1+2K}{2E}$ with finite velocity $\bar{H}_T|_{T=T_e} = -\frac{E}{K}$ for Bi $\to 0$ and at $T_e = \frac{1+2K+\text{Bi}K}{2E}$ with the same velocity for Bi > 0, as in Fig. 19(a). Comparing the two T_e, one notices that, in addition to latent heat consumption, the latter contains the effect of the ambient cooling and thus takes more time to vanish. With Bi $\to 0$ or Bi > 0, $\bar{J}$ increases from $\bar{J}_1$ or $\bar{J}_2$ at $T = 0$ to K^{-1} at T_e [see Fig. 19(b)] and singularity again occurs since the layer has already disappeared at T_e. In addition, $\bar{\Theta}_w - \bar{\Theta}_I$ decreases from $\Delta\Theta_2$ and $\Delta\Theta_1$, respectively, for Bi $\to 0$ and Bi > 0 at $T = 0$ to zero at T_e [see Fig. 19(c)] and $\Delta\Theta_1 > \Delta\Theta_2$ again results from ambient cooling. If $K \to \infty$, $\bar{J} = 0$
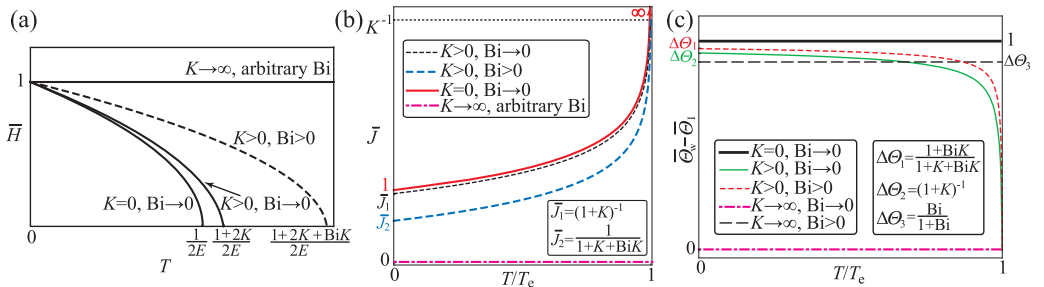

FIG. 19. Generalized basic-state behavior for (a) $\bar{H}$, (b) $\bar{J}$, and (c) $\bar{\Theta}_w - \bar{\Theta}_I$. In (b) and (c) time is scaled with T_e. In (b) the horizontal dotted line corresponding to K^{-1} denotes the value of $\bar{J}_{1,2}$ at $T = T_e$.

and the thickness remains unity [see Figs. 19(a) and 19(b)]; with, in addition, Bi → 0 the surface is insulating and heat conduction is fast enough that the film is isothermal; with Bi > 0 the ambient cooling gives rise to a steady-state temperature difference of $\Delta\Theta_3$ [see Fig. 19(c)].

APPENDIX B: LEADING-ORDER SOLUTION OF RESCALED GOVERNING SYSTEM

Here we detail the $O(1)$ solution leading to Eq. (21). First, we find the evaporative flux and temperature profile by integrating Eq. (19) subject to $\Theta_0 = 1$ and Eqs. (20b) and (20e),

$$J_0(\xi,\tau) = [K + (1 + \mathrm{Bi}K)H]^{-1}, \tag{B1}$$

$$\Theta_0(\xi,\zeta,\tau) = 1 - (1 + \mathrm{Bi}K)[K + (1 + \mathrm{Bi}K)H]^{-1}\zeta. \tag{B2}$$

Then $\Theta_I = [1 + (\mathrm{Bi} + K^{-1})H]^{-1}$. This reflects the influences of deformation, nonequilibrium, and convective and conductive heat losses on Θ_I, which will be lower than that of the model with $\frac{k_{\mathrm{th},g}}{k_{\mathrm{th}}} \to 0$ due to additional ambient cooling that can increase the temperature difference across the layer, thus favoring buoyancy convection. Interestingly, the coefficient $(\mathrm{Bi} + K^{-1})$ appears to coincide with the effective Biot number $\mathrm{Bi}_{\mathrm{eff}} = \alpha_I k$ in Ref. [12], if $p_s(\theta_I) = \rho_g R_g \theta_I / M_w$. This also makes the physical meaning of $\tilde{K}$ more explicit and confirms the effectiveness of the interfacial energy balance described by Eq. (20b). Solving Eq. (17) with Eqs. (20c), (B1), and (B2), one obtains the pressure profile

$$P_0 = \tfrac{3}{2}\bar{E}^2\bar{D}^{-1}J_0^2 - 3\bar{\Sigma}_0 H_{\xi\xi} + \bar{G}(H - \zeta) + \bar{R}\,\mathrm{Pr}^{-1}(H - \zeta)\big[\tfrac{1}{2}(H + \zeta)f - 1\big]. \tag{B3}$$

Equation (B3) consists jointly of vapor recoil and Laplace (or capillary) pressure on the free surface, as well as the effects of hydrostatic pressure and buoyancy in the bulk. Substituting it into Eq. (16) and integrating in ζ, one finds the x component of velocity as

$$U_0 = \Lambda\big(\tfrac{1}{2}\zeta^2 - H\zeta\big) - \tfrac{1}{6}\bar{R}\mathrm{Pr}^{-1}f_\xi\big(\tfrac{1}{4}\zeta^4 - H^3\zeta\big) + 2\bar{M}\mathrm{Pr}^{-1}(Hf)_\xi\zeta, \tag{B4}$$

with $\Lambda = -3\bar{E}^2\bar{D}^{-1}H_\xi f J_0^2 - 3\bar{\Sigma}_0 H_{\xi\xi\xi} + (\bar{G} - \bar{R}\,\mathrm{Pr}^{-1})H_\xi + \tfrac{1}{2}\bar{R}\,\mathrm{Pr}^{-1}(H^2 f)_\xi$. For the evolution equation, one dose not need to find z-component velocity, while it can be obtained readily by integrating the continuity equation in ζ to visualize the flow field,

$$W_0 = -\Lambda_\xi\big(\tfrac{1}{6}\zeta^3 - \tfrac{1}{2}H\zeta^2\big) + \tfrac{1}{2}\Lambda H_\xi\zeta^2 + \tfrac{1}{12}\bar{R}\mathrm{Pr}^{-1}f_{\xi\xi}\big(\tfrac{1}{10}\zeta^5 - H^3\zeta^2\big)$$
$$- \tfrac{1}{4}\bar{R}\mathrm{Pr}^{-1}H^2 H_\xi f_\xi\zeta^2 - \bar{M}\mathrm{Pr}^{-1}(Hf)_{\xi\xi}\zeta^2. \tag{B5}$$

Then a stream function ψ can be presented with the primitive variables

$$\psi(X,Z,T) = \Lambda\big(\tfrac{1}{6}Z^3 - \tfrac{1}{2}HZ^2\big) - \tfrac{1}{12}\mathrm{Gr}f_X\big(\tfrac{1}{10}Z^5 - H^3Z^2\big) + \mathrm{Ma}\,\mathrm{Pr}^{-1}(Hf)_X Z^2. \tag{B6}$$

Taking $\zeta = H$ in Eq. (B4), we obtain the horizontal liquid velocity on the interface,

$$U_{I0}(X,T) = \tfrac{1}{2}H^2\big[3E^2 D^{-1}H_X f J_0^2 + 3\Sigma_0 H_{XXX} - (G - \mathrm{Gr})H_X - \tfrac{1}{2}\mathrm{Gr}(H^2 f)_X\big]$$
$$+ \tfrac{1}{8}\mathrm{Gr}f_X H^4 + 2\mathrm{Ma}\,\mathrm{Pr}^{-1}(Hf)_X H. \tag{B7}$$

In Eqs. (B6) and (B7) the substitutions $(\bar{E}, \bar{D}, \bar{\Sigma}_0, \bar{G}, \bar{R}) \to (E, D, \Sigma_0, G, \mathrm{Ra})$ and $(\xi, \zeta, \tau) \to (X, Z, T)$ are made. With these solutions, all the flow-field variables are related to H. Finally, one substitutes Eqs. (B1) and (B4) into Eq. (18) to obtain Eq. (21).

APPENDIX C: GRADIENT DYNAMICS FORM OF EVOLUTION EQUATION

Here we discuss the related issues for the variational structure of an evolution equation, which are of fundamental interest and have been studied in Refs. [3,77,78] for volatile cases and Refs. [25,35,50,55,61,67,73] for nonvolatile cases, following Mitlin [79], who first put a dewetting

film equation in the latter case into a gradient dynamics form. Now consider the general form

$$H_t = -\nabla_1 \cdot [H^3 \nabla_1 \mathscr{P}(H)] - \mathscr{J}, \tag{C1}$$

where $\mathscr{J}$ is the generalized evaporation flux, $\mathscr{J} = \mathscr{E} J_0$ in Eq. (25), and the generalized pressure $\mathscr{P}(H) = \pm I(H) + \nabla_1^2 H$ [+ (−) for $G < 0$ ($G > 0$)] with

$$I(H) = H + \mathscr{M}(1 + \mathrm{Bi}K)\left[J_0 + \frac{1}{K}\ln(HJ_0)\right] - \frac{\mathscr{D}}{2}J_0^2 + \frac{11}{120}\mathscr{G}\left(H - \frac{K^2 J_0}{1 + \mathrm{Bi}K}\right)$$
$$- \frac{3}{20}\frac{K\mathscr{G}\ln J_0}{1 + \mathrm{Bi}K} + I_0,$$

in which the integration constant I_0 is regarded as a pressure bias that in dimensional form could be related to the vapor pressure. Equation (C1) will be subject to periodic BCs on the domain $[0, l_x] \times [0, l_y]$. We study only situations with a physical thickness of $H \geqslant 0$. Multiplying (C1) by $\mathscr{P}$ and integrating by parts, one obtains the rate of dissipation

$$\frac{d\mathscr{F}}{dt} = -\int_0^{l_x}\int_0^{l_y} H^3 \|\nabla_1 \mathscr{P}\|^2 dx\,dy + \mathscr{E}\int_0^{l_x}\int_0^{l_y} J_0 \mathscr{P}\,dx\,dy, \tag{C2}$$

where $\mathscr{F}[H] = \int_0^{l_x}\int_0^{l_y}[-V(H) + \frac{1}{2}\|\nabla_1 H\|^2]dx\,dy$ is an energy functional, incorporating the surface energy of the curved free interface (due to surface tension) and the "potential" energy

$$V(H) = \pm \int I(H)dH = \pm\left[\frac{1}{2}H^2 + \frac{(1 + \mathrm{Bi}K)\mathscr{M}}{K}H\ln(HJ_0) + \frac{\mathscr{D}J_0}{2(1 + \mathrm{Bi}K)}\right.$$
$$\left. + \frac{11}{240}\mathscr{G}H^2 - \frac{3}{20}\frac{K\mathscr{G}H}{1 + \mathrm{Bi}K}(1 + \ln J_0) - \frac{7}{120}\frac{K^2\mathscr{G}\ln J_0}{(1 + \mathrm{Bi}K)^2} + I_0 H\right]. \tag{C3}$$

Here $V(H)$ includes component energies associated with gravity, Marangoni stress, vapor recoil, and buoyancy; the last linear term accounts for an energy offset towards the liquid or gas phase; and the arbitrary constant of integration is set to zero without loss of generality. It is noted that $\lim_{H\to\infty}|V(H)| = \infty$ and $\lim_{H\to 0}|V(H)| = \frac{1}{2(1 + \mathrm{Bi}K)}[\frac{\mathscr{D}}{K} + \frac{7K^2\mathscr{G}\ln K}{60(1 + \mathrm{Bi}K)}]$.

To write Eq. (C1) as gradient dynamics, we let $\mathscr{E} = 0$ (mass conserved) since $\mathscr{J} = \mathscr{E}J_0$ breaks such a structure [3] and then recast it into a CH type [80] in the context of pattern formation in liquid layers (see, e.g., Refs. [25,28,35,79]), although with a different potential,

$$H_t = \nabla_1 \cdot \left[Q_c(H)\nabla_1\left(\frac{\delta\mathscr{F}}{\delta H}\right)\right], \tag{C4}$$

where $Q_c(H) = H^3$ is the mobility function for the conserved part, the first variation $\frac{\delta\mathscr{F}}{\delta H} = -\mathscr{P}$. As $\frac{d\mathscr{F}}{dt} \leqslant 0$, $\mathscr{F}$ is a Lyapunov functional for Eq. (C1) with $\mathscr{E} = 0$. We next incorporate two relevant forms of the nonconserved part used in the literature.

(i) Motivated by the evaporation term in Refs. [3,53,75], e.g., Eq. (12) in Ref. [3], we consider a special case of the variational-form flux $\mathscr{J}_a = \mathscr{E}J_0\frac{\delta\mathscr{F}}{\delta H}$, which is expected in the case of evaporation limited by the phase transition at the interface. Equation (C2) then becomes

$$\frac{d\mathscr{F}}{dt} = -\int_0^{l_x}\int_0^{l_y} H^3\|\nabla_1\mathscr{P}\|^2 dx\,dy - \mathscr{E}\int_0^{l_x}\int_0^{l_y} J_0\mathscr{P}^2 dx\,dy \leqslant 0 \quad \text{for } \mathscr{E} \geqslant 0. \tag{C5}$$

The interface thus evolves monotonically in such a way that $\mathscr{F}$ is strictly nonincreasing in t towards its minimum. This confirms the flux $\mathscr{J}_a$ with $\mathscr{E} > 0$ to be consistent with the energy functional underlying the conserved part of the dynamics. Further, Eq. (C1) can take a gradient dynamics form

$$H_t = \nabla_1 \cdot \left[Q_c(H)\nabla_1\left(\frac{\delta\mathscr{F}}{\delta H}\right)\right] - Q_{\mathrm{nc}}(H)\frac{\delta\mathscr{F}}{\delta H}, \tag{C6}$$

where $Q_{\mathrm{nc}}(H) = \mathscr{E} J_0$ is the mobility for the nonconserved part and the contribution of vapor pressure I_0 has been incorporated into $\mathscr{F}$ [78]. It should be mentioned that the physics included in $\mathscr{J}_a$ here is very different from the model by Ajaev and Homsy [75], although they look the same. In the latter, only capillarity and wettability enter evaporation, however, our $\mathscr{J}_a$ includes the influences of curvature, thermocapillarity, gravity, and vapor recoil on the local pressure, but not wettability since the liquid layer is thick compared to the range of disjoining pressure [28,50,54]. While when $\mathscr{E} < 0$ more complicated dynamics can arise, as suggested by Eq. (C5), $\mathscr{F}$ is no longer guaranteed to be monotonically decreasing. Equations (C5) and (C6) fall within the general framework in Ref. [77].

(ii) With $\mathscr{J}_b = \mathscr{E}(H - 1)$, a simplified functional $F[H] = \mathscr{F}_{\mathrm{GL}}[H] + \mathscr{F}_{\mathrm{ev}}[H]$ for an extended CH equation, showing nonlinear behaviors similar to a reduced version of Eq. (C1), has been stated in Eq. (13) of Ref. [28], with the Ginzburg-Landau free energy $\mathscr{F}_{\mathrm{GL}}$ and a simplified potential $\mathscr{F}_{\mathrm{ev}}$ accounting for mass loss [28]. The evaporation term is a distributed influx or outflux modeled by a point charge, which allows the system to remain permanently out of equilibrium. The dispersion relation in Ref. [28] is qualitatively different from that of Eq. (C6) (see Fig. 4 in [77]). Consequently, the special simplified model cannot be written in the form of Eq. (C6) with the same $\mathscr{F}$ in both terms. That is, it is not a gradient dynamics.

For Eq. (C1) (even in a reduced version) with a more general nonconserved part whether the gradient dynamics approach can be extended to systematically incorporate such a flux is still an open question [77,78]. We conjecture that if possible the underlying $\mathscr{F}_{\mathrm{ev}}[H]$ could take a more sophisticated *nonlocal* form, because the evaporative flux could be a nonlocal function of the whole interface configuration.

Finally, we restrict ourselves to the conserved system. If a stationary solution of Eq. (C4) exists, it must minimize $\mathscr{F}$ and obey the mass conservation condition $\int_0^{l_x} \int_0^{l_y} H \, dx \, dy = l_x l_y$. This solution could be found by minimizing the modified functional

$$\mathscr{L}[H] = \int_0^{l_x} \int_0^{l_y} \left[-V(H) + \tfrac{1}{2}\|\nabla_1 H\|^2 + \lambda_{\mathrm{L}} H \right] dx \, dy, \tag{C7}$$

where λ_{L} is the Lagrange multiplier. This means that the stationary solution should satisfy the Euler-Lagrange equation for $\mathscr{L}[H]$,

$$\nabla_1^2 H + V_H - \lambda_{\mathrm{L}} = 0. \tag{C8}$$

This is equivalent to searching for the steady-state solution of the dynamical system $H_t = \nabla_1^2 H + V_H - \lambda_{\mathrm{L}}(t)$, where mass conservation is imposed by $\lambda_{\mathrm{L}}(t) = (l_x l_y)^{-1} \int_0^{l_x} \int_0^{l_y} V_H dx \, dy$. Therefore, the solutions of Eq. (C8), obtained by numerically solving the time-dependent problem as $t \to \infty$, are not only stationary solutions of Eq. (C4) but also stable nonrupture, if two conditions are met: (i) $\pm V(H)$ has a lower bound [$+ (-)$ for $G < 0$ ($G > 0$)] and (ii) $\pm V(H)$ attains a minimum at $H > 0$. Note that if one is only concerned about the localized stable stationary nonrupture (SSNR) states instead of the transient behavior of the system, the constrained optimization problem is more numerically efficient than solving Eq. (C4).

Figure 20 shows the typical structure of potential $\pm V$ with $I_0 < 0$ for different values of $\mathscr{M}$ and $\mathscr{D}$. The curves may have two minima if $|\mathscr{M}| \in (\mathscr{M}_l, \mathscr{M}_u)$, where $\mathscr{M}_l$ and $\mathscr{M}_u$ are parametrized by $K, \mathscr{G}, \mathscr{D}$, Bi, and I_0 [e.g., in Fig. 20(a) when $0.83 < |\mathscr{M}| < 5.6$ for $\mathscr{D} = 1$], one global minimum achieved at a finite H if $|\mathscr{M}| < \mathscr{M}_l$, or one global minimum at $H = 0$ if $|\mathscr{M}| > \mathscr{M}_u$. With the given parameters, it is found that the conditions (i) and (ii) are met if $0 < |\mathscr{M}| < 5.6$ and $0 < |\mathscr{M}| < 3$ for $|\mathscr{D}| = 1$ in Figs. 20(a) and 20(b), respectively. The potential well allows the existence of SSNR solutions which lie in its basin of attraction; if disturbed slightly, they can be restored at the bottom. Physically, we demonstrate that from Fig. 20(a) the destabilizing effects of RTI and vapor recoil can be suppressed by the adequate stabilizing effect of thermocapillarity in the case of a condensing layer hanging from a cooled substrate and that from Fig. 20(b) the destabilizations of vapor recoil and thermocapillarity can be balanced by hydrostatic pressure in the case of an evaporating layer lying on a heated substrate, while spontaneous rupture should not be surprising in the evaporation
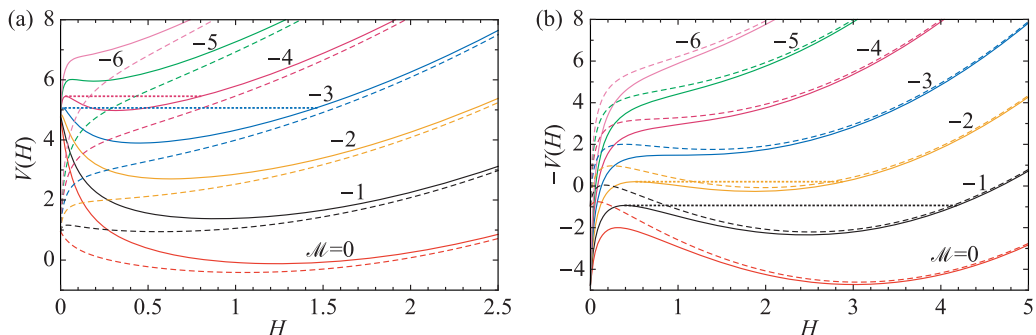
FIG. 20. Potential energy for $K = 0.1$, $|\mathscr{G}| = 0.2$, $\mathrm{Bi} = 0.5$, $|\mathscr{D}| = 0.2$ (dashed line) or 1 (solid line), and different values of $\mathscr{M}$ showing global and local minima: (a) $V(H)$ for condensing layers hanging from a cooled substrate ($\mathscr{D}, \mathscr{G} > 0$) with $I_0 = -1$ and (b) $-V(H)$ for evaporating layers lying on a heated substrate with $I_0 = -3$. The horizontal dotted lines indicate the potential wells for several curves.

simulation because of the additional mass loss. Furthermore, the order-of-magnitude variation in the vapor recoil effect is only significant for $|V(H)|$ as $H \to 0$. The minimum at $H = 0$ suggests that the solution is in the form of drops separated by "dry spots". In addition, the value of I_0 (which may be greater than, less than, or equal to zero) depends on the dynamics of the system and BCs. We take the *a priori* values to explain the possible structures of V and no attempt is made to determine I_0 in the brief discussion.

[1] A. Oron, S. H. Davis, and S. G. Bankoff, Long-scale evolution of thin liquid films, Rev. Mod. Phys. **69**, 931 (1997).

[2] R. V. Craster and O. K. Matar, Dynamics and stability of thin liquid films, Rev. Mod. Phys. **81**, 1131 (2009).

[3] U. Thiele, Patterned deposition at moving contact lines, Adv. Colloid Interface Sci. **206**, 399 (2014).

[4] P. Cerisier, C. Jamond, J. Pantaloni, and C. Pérez-García, Stability of roll and hexagonal patterns in Bénard-Marangoni convection, Phys. Fluids **30**, 954 (1987).

[5] K. Eckert, M. Bestehorn, and A. Thess, Square cells in surface-tension-driven Bénard convection: Experiment and theory, J. Fluid Mech. **356**, 155 (1998).

[6] J. R. A. Pearson, On convection cells induced by surface tension, J. Fluid Mech. **4**, 489 (1958).

[7] S. J. VanHook, M. F. Schatz, W. D. McCormick, J. B. Swift, and H. L. Swinney, Long-Wavelength Instability in Surface-Tension-Driven Bénard Convection, Phys. Rev. Lett. **75**, 4397 (1995).

[8] S. J. VanHook, M. F. Schatz, J. B. Swift, W. D. McCormick, and H. L. Swinney, Long-wavelength surface-tension-driven Bénard convection: Experiment and theory, J. Fluid Mech. **345**, 45 (1997).

[9] N. Zhang, in *Surface Tension-Driven Flows and Applications*, edited by R. Savino (Research Signpost, Kerala, 2006), Chap. 6, pp. 147–171.

[10] W. Guo and R. Narayanan, Interfacial instability due to evaporation and convection: Linear and nonlinear analyses, J. Fluid Mech. **650**, 363 (2010).

[11] J. C. Berg, M. Boudart, and A. Acrivos, Natural convection in pools of evaporating liquids, J. Fluid Mech. **24**, 721 (1966).

[12] F. Chauvet, S. Dehaeck, and P. Colinet, Threshold of Bénard-Marangoni instability in drying liquid films, Europhys. Lett. **99**, 34001 (2012).

[13] M. J. Block, Surface tension as the cause of Bénard cells and surface deformation in a liquid film, Nature (London) **178**, 650 (1956).

[14] D. A. Nield, Surface tension and buoyancy effects in cellular convection, J. Fluid Mech. **19**, 341 (1964).

[15] J. Margerit, P. Colinet, G. Lebon, C. S. Iorio, and J. C. Legros, Interfacial nonequilibrium and Bénard-Marangoni instability of a liquid-vapor system, Phys. Rev. E **68**, 041601 (2003).

[16] B. Haut and P. Colinet, Surface-tension-driven instabilities of a pure liquid layer evaporating into an inert gas, J. Colloid Interface Sci. **285**, 296 (2005).

[17] L. E. Scriven and C. V. Sternling, On cellular convection driven by surface-tension gradients: Effects of mean surface tension and surface viscosity, J. Fluid Mech. **19**, 321 (1964).

[18] K. A. Smith, On convective instability induced by surface-tension gradients, J. Fluid Mech. **24**, 401 (1966).

[19] J. P. Burelbach, S. G. Bankoff, and S. H. Davis, Steady thermocapillary flows of thin liquid layers. II. Experiment, Phys. Fluids A **2**, 322 (1990).

[20] A. A. Golovin, A. A. Nepomnyashchy, and L. M. Pismen, Interaction between short-scale Marangoni convection and long-scale deformational instability, Phys. Fluids **6**, 34 (1994).

[21] A. A. Golovin, A. A. Nepomnyashchy, and L. M. Pismen, Nonlinear evolution and secondary instabilities of Marangoni convection in a liquid-gas system with deformable interface, J. Fluid Mech. **341**, 317 (1997).

[22] A. A. Golovin, A. A. Nepomnyashchy, and L. M. Pismen, Nonpotential effects in nonlinear dynamics of Marangoni convection, Int. J. Bifurcat. Chaos **12**, 2487 (2002).

[23] M. G. Velarde, A. A. Nepomnyashchy, and M. Hennenberg, Onset of oscillatory interfacial instability and wave motions in Bénard layers, Adv. Appl. Mech. **37**, 167 (2001).

[24] S. Chandrasekhar, *Hydrodynamic and Hydromagnetic Stability* (Oxford University Press, London, 1961).

[25] A. Oron and P. Rosenau, Formation of patterns induced by thermocapillarity and gravity, J. Phys. (France) II **2**, 131 (1992).

[26] S. G. Yiantsios and B. G. Higgins, Rayleigh-Taylor instability in thin viscous films, Phys. Fluids A **1**, 1484 (1989).

[27] M. Fermigier, L. Limat, J. E. Wesfreid, P. Boudinet, and C. Quilliet, Two-dimensional patterns in Rayleigh-Taylor instability of a thin layer, J. Fluid Mech. **236**, 349 (1992).

[28] M. Bestehorn and D. Merkt, Regular Surface Patterns on Rayleigh-Taylor Unstable Evaporating Films Heated from Below, Phys. Rev. Lett. **97**, 127802 (2006).

[29] K. C. D. Hickman, Surface behavior in the pot still, Ind. Eng. Chem. **44**, 1892 (1952).

[30] H. J. Palmer, The hydrodynamic stability of rapidly evaporating liquids at reduced pressure, J. Fluid Mech. **75**, 487 (1976).

[31] J. P. Burelbach, S. G. Bankoff, and S. H. Davis, Nonlinear stability of evaporating/condensing liquid films, J. Fluid Mech. **195**, 463 (1988).

[32] T. Wei and F. Duan, Interfacial stability and self-similar rupture of evaporating liquid layers under vapor recoil, Phys. Fluids **28**, 124106 (2016).

[33] A. Prosperetti and M. S. Plesset, The stability of an evaporating liquid surface, Phys. Fluids **27**, 1590 (1984).

[34] S. W. Joo, S. H. Davis, and S. G. Bankoff, Long-wave instabilities of heated falling films: Two-dimensional theory of uniform layers, J. Fluid Mech. **230**, 117 (1991).

[35] A. Oron, Three-Dimensional Nonlinear Dynamics of Thin Liquid Films, Phys. Rev. Lett. **85**, 2108 (2000).

[36] O. E. Shklyaev and E. Fried, Stability of an evaporating thin liquid film, J. Fluid Mech. **584**, 157 (2007).

[37] O. Ozen and R. Narayanan, The physics of evaporative and convective instabilities in bilayer systems: Linear theory, Phys. Fluids **16**, 4644 (2004).

[38] E. Sultan, A. Boudaoud, and M. B. Amar, Evaporation of a thin film: Diffusion of the vapour and Marangoni instabilities, J. Fluid Mech. **543**, 183 (2005).

[39] K. Kanatani and A. Oron, Nonlinear dynamics of confined thin liquid-vapor bilayer systems with phase change, Phys. Fluids **23**, 032102 (2011).

[40] M. J. Tan, S. G. Bankoff, and S. H. Davis, Steady thermocapillary flows of thin liquid layers. I. Theory, Phys. Fluids A **2**, 313 (1990).

[41] A. Oron and P. Rosenau, On a nonlinear thermocapillary effect in thin liquid layers, J. Fluid Mech. **273**, 361 (1994).

[42] W. Boos and A. Thess, Cascade of structures in long-wavelength Marangoni instability, Phys. Fluids **11**, 1484 (1999).

[43] J. T. Kimball, J. C. Hermanson, and J. S. Allen, Experimental investigation of convective structure evolution and heat transfer in quasi-steady evaporating liquid films, Phys. Fluids **24**, 052102 (2012).

[44] T. P. Witelski and A. J. Bernoff, Stability of self-similar solutions for van der Waals driven thin film rupture, Phys. Fluids **11**, 2443 (1999).

[45] T. P. Witelski and A. J. Bernoff, Dynamics of three-dimensional thin film rupture, Physica D **147**, 155 (2000).

[46] D. Vaynblat, J. R. Lister, and T. P. Witelski, Symmetry and self-similarity in rupture and pinchoff: A geometric bifurcation, Eur. J. Appl. Math. **12**, 209 (2001).

[47] D. Tseluiko, J. Baxter, and U. Thiele, A homotopy continuation approach for analysing finite-time singularities in thin liquid films, IMA J. Appl. Math. **78**, 762 (2013).

[48] M. C. Dallaston, D. Tseluiko, Z. Zheng, M. A. Fontelos, and S. Kalliadasis, Self-similar finite-time singularity formation in degenerate parabolic equations arising in thin-film flows, Nonlinearity **30**, 2647 (2017).

[49] S. Shklyaev, A. V. Straube, and A. Pikovsky, Superexponential droplet fractalization as a hierarchical formation of dissipative compactons, Phys. Rev. E **82**, 020601 (2010).

[50] U. Thiele and E. Knobloch, Thin liquid films on a slightly inclined heated plate, Physica D **190**, 213 (2004).

[51] M. C. Dallaston, M. A. Fontelos, D. Tseluiko, and S. Kalliadasis, Discrete Self-Similarity in Interfacial Hydrodynamics and the Formation of Iterated Structures, Phys. Rev. Lett. **120**, 034505 (2018).

[52] P. Rosenau and J. M. Hyman, Compactons: Solitons with Finite Wavelength, Phys. Rev. Lett. **70**, 564 (1993).

[53] H. Ji and T. P. Witelski, Finite-time thin film rupture driven by modified evaporative loss, Physica D **342**, 1 (2017).

[54] A. Oron, Nonlinear dynamics of three-dimensional long-wave Marangoni instability in thin liquid films, Phys. Fluids **12**, 1633 (2000).

[55] A. v. B. Lopes, U. Thiele, and A. L. Hazel, On the multiple solutions of coating and rimming flows on rotating cylinders, J. Fluid Mech. **835**, 540 (2018).

[56] F. Doumenc, T. Boeck, B. Guerrier, and M. Rossi, Transient Rayleigh-Bénard-Marangoni convection due to evaporation: A linear non-normal stability analysis, J. Fluid Mech. **648**, 521 (2010).

[57] D. M. Anderson and S. H. Davis, The spreading of volatile liquid droplets on heated surfaces, Phys. Fluids **7**, 248 (1995).

[58] I. L. Kliakhandler, S. H. Davis, and S. G. Bankoff, The effect of heat conduction in the vapor on the dynamics of downflowing condensate, Phys. Fluids **14**, 150 (2002).

[59] M. B. Williams and S. H. Davis, Nonlinear theory of film rupture, J. Colloid Interface Sci. **90**, 220 (1982).

[60] S. Krishnamoorthy, B. Ramaswamy, and S. W. Joo, Spontaneous rupture of thin liquid films due to thermocapillarity: A full-scale direct numerical simulation, Phys. Fluids **7**, 2291 (1995).

[61] A. Oron and S. G. Bankoff, Dewetting of a heated surface by an evaporating liquid film under conjoining/disjoining pressures, J. Colloid Interface Sci. **218**, 152 (1999).

[62] P. L. Garcia-Ybarra, J. L. Castillo, and M. G. Velarde, A nonlinear evolution equation for Bénard-Marangoni convection with deformable boundary, Phys. Lett. A **122**, 107 (1987).

[63] A. Oron and P. Rosenau, Evolution of the coupled Bénard-Marangoni convection, Phys. Rev. A **39**, 2063 (1989).

[64] C. Normand, Y. Pomeau, and M. G. Velarde, Convective instability: A physicist's approach, Rev. Mod. Phys. **49**, 581 (1977).

[65] K. Kanatani, Effects of convection and diffusion of the vapour in evaporating liquid films, J. Fluid Mech. **732**, 128 (2013).

[66] See Supplemental Material at http://link.aps.org/supplemental/10.1103/PhysRevFluids.3.034001 for the evolution of pendent and sessile layers.

[67] R. J. Deissler and A. Oron, Stable Localized Patterns in Thin Liquid Films, Phys. Rev. Lett. **68**, 2948 (1992).

[68] A. Orell and S. G. Bankoff, Formation of a dry spot in a horizontal liquid film heated from below, Int. J. Heat Mass Transfer **14**, 1835 (1971).

[69] H. Jeffreys, The surface elevation in cellular convection, Q. J. Mech. Appl. Math. **4**, 283 (1951).

[70] M. Bestehorn, Phase and amplitude instabilities for Bénard-Marangoni convection in fluid layers with large aspect ratio, Phys. Rev. E **48**, 3622 (1993).

[71] P. Kavehpour, B. Ovryn, and G. H. McKinley, Evaporatively-driven Marangoni instabilities of volatile liquid films spreading on thermally conductive substrates, Colloids Surf. A **206**, 409 (2002).

[72] B. Cabral and L. C. Leedom, in *Proceedings of the 20th Annual Conference on Computer Graphics and Interactive Techniques, Anaheim, 1993* (ACM, New York, 1993), p. 263.

[73] R. S. Laugesen and M. C. Pugh, Properties of steady states for thin film equations, Eur. J. Appl. Math. **11**, 293 (2000).

[74] B. B. Mandelbrot, *The Fractal Geometry of Nature* (Freeman, New York, 1983).

[75] V. S. Ajaev and G. M. Homsy, Steady vapor bubbles in rectangular microchannels, J. Colloid Interface Sci. **240**, 259 (2001).

[76] E. W. Lemmon, M. L. Huber, and M. O. McLinden, *NIST Standard Database 23*, Version 8.0 (NIST, Gaithersburg, 2007).

[77] U. Thiele, Thin film evolution equations from (evaporating) dewetting liquid layers to epitaxial growth, J. Phys.: Condens. Matter **22**, 084019 (2010).

[78] U. Thiele, A. J. Archer, and L. M. Pismen, Gradient dynamics models for liquid films with soluble surfactant, Phys. Rev. Fluids **1**, 083903 (2016).

[79] V. S. Mitlin, Dewetting of solid surface: Analogy with spinodal decomposition, J. Colloid Interface Sci. **156**, 491 (1993).

[80] J. W. Cahn and J. E. Hilliard, Free energy of a nonuniform system. I. Interfacial free energy, J. Chem. Phys. **28**, 258 (1958).